

Dynamics of neutral cluster growth and cluster ion fragmentation for toluene/water, aniline/argon, and 4-fluorostyrene/argon clusters: Covariance mapping of the mass spectral data

M. Foltin, G. J. Stueber, and E. R. Bernstein

Citation: *The Journal of Chemical Physics* **109**, 4342 (1998); doi: 10.1063/1.477037

View online: <http://dx.doi.org/10.1063/1.477037>

View Table of Contents: <http://aip.scitation.org/toc/jcp/109/11>

Published by the *American Institute of Physics*

COMPLETELY

REDESIGNED!



**PHYSICS
TODAY**

Physics Today Buyer's Guide
Search with a purpose.

Dynamics of neutral cluster growth and cluster ion fragmentation for toluene/water, aniline/argon, and 4-fluorostyrene/argon clusters: Covariance mapping of the mass spectral data

M. Foltin, G. J. Stueber, and E. R. Bernstein

Department of Chemistry, Colorado State University, Fort Collins, Colorado 80523-1872

(Received 20 March 1998; accepted 9 June 1998)

Neutral cluster growth and ionic cluster fragmentation are studied for toluene/water (TW_n), aniline/argon ($AnAr_n$), and 4-fluorostyrene/argon ($FSAr_n$). Clusters are created in a supersonic expansion and ionized by both one-color and two-color (near threshold) resonance enhanced laser ionization. Toluene/water clusters are known to fragment subsequent to ionization by loss of water molecules or by proton transfer and loss of a benzyl radical. This system is selected to test the applicability of covariance mapping techniques to investigate the fragmentation behavior of singly charged cluster ions. To explore sensitivity of the parent ion/fragment ion correlation coefficient to cluster fragmentation, correlation coefficients are measured as a function of ionization photon energy as thresholds for the various fragmentation processes are scanned. For TW_3^+ parent ions, correlation coefficients correctly reflect switching between the benzyl radical loss and water loss fragmentation channels as the photon energy is increased. For $T_2W_n^+$ cluster ions, fragmentation contributes only about 20% to the correlation coefficient—the other 80% contribution is due to neutral cluster growth. The growth-dominated correlation coefficients scale approximately with the square root of the product of the two ion signal intensities and linearly with the ionization laser intensity, and therefore are not good relative measures of correlations between ions and signals of different intensities. A normalized covariance (covariance/product of signal intensities) is introduced to eliminate this dependence. The laser intensity [$\sim(\text{signal product})^{1/2}$] independent component of the normalized covariance arises from ion correlation due to neutral cluster growth and the laser intensity dependent component of the normalized covariance arises from ion correlation due to cluster ion fragmentation. These findings are applied to study the cluster growth dynamics of $AnAr_n$ and $FSAr_n$ clusters. Covariance mapping shows that the broad intensity maxima in the mass spectrum of $FSAr_n$ clusters are not caused by fragmentation but can be attributed to neutral cluster growth. The observed neutral cluster distribution appears to be a superposition of three broad, overlapping, log-normal-like distributions peaking around cluster sizes $n = 4, 8, 20$. The difference between the overall shapes of the $AnAr_n$ and $FSAr_n$ mass distributions appears to be due to faster dimer and cluster growth kinetics for the $FSAr_n$ cluster system. The growth kinetics for the latter two cluster systems can be fully explained and modeled by a simple closed form algebraic kinetic equation that depends on three parameters: dimer growth rate, overall cluster growth rate, and a cluster growth cross section that scales with cluster size. © 1998 American Institute of Physics. [S0021-9606(98)00135-4]

I. INTRODUCTION

In the mass spectroscopy of clusters and polyatomic molecules, ion fragmentation is often a serious problem even if careful threshold energy ionization is pursued: Franck–Condon factors for the ionization can require that the ions are created with excess vibrational energy. Two questions arise for a mass spectrum produced with excess ion energy: (1) Does the observed mass spectrum reflect the neutral distribution of species? (2) If cluster ion fragmentation has occurred, what are the pathways? Ionic fragmentation on the tens of microseconds time scale (metastable fragmentation) can be determined in a reflectron-time-of-flight or a double focusing sector field mass spectrometer; however, no simple way exists to correlate the fragmenting ions in the ion extraction region of a mass spectrometer in the first few hun-

dred nanoseconds following ionization. Additionally, parent/fragment ion associations must be made to help identify mass resolved excitation spectra in a complex fragmenting cluster system.

Time-of-flight mass spectroscopy (TOFMS) is frequently employed in cluster studies because it can obtain a complete mass spectrum of the sample in a single ionization (laser) pulse. A TOF mass spectrometer has a large throughput and a final mass spectrum for a cluster system is typically acquired by averaging the signals from many ($\sim 10^3$) ionization pulses to achieve good signal to noise ratios. The averaging process, however, also results in the loss of considerable important information contained in each individual trace or scan of the mass spectrum. In particular, some ions appear in these scans in association or antiassociation with other ions. It is such information that can suggest fragmentation

parent/daughter and growth relationships between cluster ions.¹⁻⁶ Houk and co-workers were among the first to test for these ion associations by employing the chi-square (χ^2) test and computing correlation coefficients (γ) for ion signals in different mass channels for a collection of individual single pulse TOF mass spectra.¹ Pairs of ions with γ larger than some critical value γ_0 (corresponding to a certain confidence level) are considered associated. These investigators studied CsI, YBa₂Cu₃O₇, (VO)₂P₂O₇, and β -VOPO₄ cluster systems generated by laser ablation. They showed that ion formation and fragmentation pathways and mechanisms could be uncovered by such covariance mapping techniques. Of particular interest for our studies is the behavior of (VO)₂P₂O₇ and VOPO₄ systems.^{1(b)} Their mass spectra are very similar, but their ion association maps are very different. Thus while the overall ablation process yields similar mass spectra, very different sets of growth kinetics give rise to these mass spectral intensities.

Contemporaneous with the Houk group studies are those by Frasninski *et al.*,² who employed covariance mapping to obtain "momentum" maps of fragmenting multiply charged ions during a Coulomb explosion. These maps can be employed to reveal kinetic energy release in fragmentation processes for these ions. A number of groups have followed these two paths and employed the covariance map for momentum and correlated ion studies. Correlation of neutral fragments from photodissociation of mass selected cluster ions is another application of the covariance mapping technique. Systems as diverse as argon clusters,³ ammonia clusters,⁴ CF₄,⁵ and laser ablated plumes of high temperature superconductors,^{6(a),6(b)} and Pb(Ti_{0.48}Zr_{0.52})O₃ ferroelectrics^{6(c)} have been investigated.

To explore the suitability of this technique for the study of neutral cluster growth and ionic cluster fragmentation behavior of singly charged van der Waals clusters, we first study the toluene/water cluster system. The toluene/water cluster system is known to undergo intensive, but energy controlled fragmentation processes upon ionization: the threshold for ionization and various fragmentation pathways can be scanned by tuning the laser generated ionization wavelength. This approach, combined with simple computer modeling and ionization laser intensity dependence studies, allows one to uncouple the correlation component due to fragmentation from other contributions to the ion correlation, including those from neutral cluster growth and instrumental effects. In some instances, one can expose individual fragmentation pathways.

The potential and limitations for the covariance mapping technique to expose these pathways are discussed in this report. These findings are then employed to interpret the mass spectra of aniline/argon (AnAr_{*n*}) and 4-fluorostyrene/argon (FSAr_{*n*}) van der Waals cluster systems. Bréchnignac and co-workers⁷ observe that these two similar solute/solvent systems have very different mass spectral intensity patterns under one-color, two-photon ionization conditions: AnAr_{*n*} ion signal intensities decrease with increase in cluster size *n*; FSAr_{*n*} cluster signals peak at local maximum for about *n* ~ 4. Under the present two-color, two-photon threshold ionization conditions, however, the AnAr_{*n*} spectrum has a glo-

bal maximum at *n* ~ 4. As the expansion backing pressure increases, the AnAr_{*n*} distribution maximum smoothly shifts to higher cluster sizes and the FSAr_{*n*} distribution develops two additional maxima at *n* ~ 8, 20. The normalized covariance matrix elements are small and are all equal for the AnAr_{*n*} clusters system, but large and positive for (FSAr_{*n*}⁺, FSAr_{*n-1*}⁺) and negative for (FSAr_{*n*}⁺, FSAr_{*n-l*}⁺) clusters, with *l* a function of *n* and backing pressure (*l* > 5). The covariances change smoothly for the FSAr_{*n*} distribution. Covariance mapping shows clearly that these threshold distributions are not associated with cluster ion fragmentation but that they are due to cluster growth patterns. Through computer modeling and simulation of cluster growth rate equations, one can demonstrate that the important growth kinetic parameters are the dimer formation rate constant and the overall clustering rate constant.

II. COVARIANCE MAPPING

The correlation coefficient $\gamma(x,y)$ is a quantity frequently used in the scientific literature to express the probability of simultaneous occurrence of two different events *x* and *y* in a sequence of observations (scans). It is derived from the covariance $C(x,y)$ defined by

$$C(x,y) = \frac{1}{n} \sum_{i=1}^n (x_i - \bar{x})(y_i - \bar{y}) \quad (1)$$

in which x_i and y_i are the numbers of occurrences (or intensities) of events *x* and *y* in the *i*th scan and

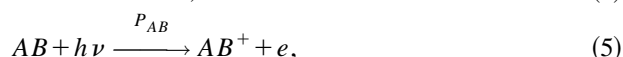
$$\bar{x} = \frac{1}{n} \sum_{i=1}^n x_i, \quad \bar{y} = \frac{1}{n} \sum_{i=1}^n y_i$$

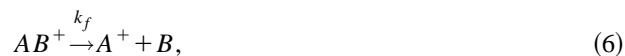
are the mean numbers of occurrences of events *x* and *y* in all scans. The correlation coefficient $\gamma(x,y)$ is a normalized form of the covariance defined by

$$\gamma(x,y) = \frac{C(x,y)}{[C(x,x)C(y,y)]^{1/2}}. \quad (2)$$

$C(x,x)$ and $C(y,y)$ are the diagonal elements of the covariance matrix and are usually referred to as the variance of *x* and *y*, respectively: σ_x , the standard deviation of *x* is given by $[C(x,x)]^{1/2}$ and likewise for σ_y . γ can assume only values in the range (-1 to +1): a value of $\gamma=0$ implies no correlation; a value of $\gamma=-1$ implies complete anticorrelation; and a value of $\gamma=1$ implies complete correlation. The advantage of characterizing covariances and correlations rather than coincidence between ions is that $C(x,y)$ and $\gamma(x,y)$ consider the arrival of more than one ion of the same species within the same scan.

To apply the covariance mapping technique to the complex neutral growth and ion fragmentation cluster systems of concern in this study, consider a sequence of cluster growth, cluster ionization, and cluster ion fragmentation reactions:





in which k_a denotes the aggregation rate, P_A is the ionization probability of cluster or molecule A , P_{AB} is the ionization probability of cluster AB , and k_f is the ion fragmentation rate. If $k_f=0$, the cluster ions A^+ and AB^+ will be correlated only through the aggregation rate Eq. (3). This correlation will be negative if fluctuations of the cluster growth rate k_a are the dominant fluctuations. If the concentration of particles A fluctuates and its fluctuations are dominant, the ions A^+ and AB^+ may be positively correlated. If the fragmentation probability k_f is nonzero, the correlation coefficient will be affected also by fluctuations of k_f and by the fluctuations of the ionization probability P_{AB} . The correlation between AB^+ and A^+ will be negative if fluctuations of k_f prevail, while it will be positive if fluctuations of P_{AB} prevail.

Since the number of AB^+ and A^+ ions will be smaller than the number of their neutral precursors (i.e., P_A and $P_{AB} < 1$), the Poisson fluctuations due to the statistical nature of the ionization and fragmentation processes will tend to be higher than those due to cluster growth. According to estimates based on the number of detected ions (~ 10 ions/mass peak/laser pulse) and estimated ionization efficiencies ($< 10\%$), fluctuations due to fragmentation would be expected to be about 30% of ion signal intensity, while those from growth should be about 10%. Hence the correlation due to cluster fragmentation should, in general, be expected to be higher than that due to cluster growth. Whether fluctuations related to cluster growth or cluster fragmentation dominate the correlations between AB^+ and A^+ will depend on the properties of the system under study and on the ionization mechanism. A more rigorous and in depth mathematical analysis of these ideas will be presented after the presentation of the toluene/water cluster correlation results.

III. EXPERIMENTAL PROCEDURES

The clusters studied in this work are created by supersonic expansion from either an R. M. Jordan Co. pulsed nozzle with a 0.8-mm-diam orifice or a cw nozzle with a 0.225 mm orifice. The pulsed nozzle yields higher signal intensities and is therefore used in most of the experiments; however, due to the sensitivity of the covariance mapping technique to pulse-to-pulse fluctuations of the nozzle effective opening area, we employ the cw nozzle to check for correlations due to nozzle fluctuations. Toluene/water clusters are made by coexpansion of toluene and water vapors at their respective room temperature vapor pressures seeded into 50 psi He in the case of the pulsed nozzle and about 7 psi He in the case of the cw nozzle. The aniline/argon and fluorostyrene/argon clusters are generated by coexpansion of the chromophore solute at its room temperature vapor pressure with ~ 50 psi Ar for the pulsed nozzle and ~ 20 psi Ar for the cw nozzle. For the study of the $AnAr_{1,2}$ clusters a 10% Ar, 90% He mixture is used as the expansion gas to reduce the number of large clusters in the supersonic beam. The molecular beam for the pulsed nozzle is first skimmed (1 mm hyperbolic skimmer) before it enters the ionization region of a commercial TOF mass spectrometer of the Wiley-McLaren design made by the R. M. Jordan Co. The cw

nozzle is mounted at the opposite side of the ion source from the pulse nozzle and its skimmed beam is ionized about 25 cm from the cw nozzle. The cw nozzle is differentially pumped and the two chambers are separated by the skimmer through which the cw beam passes.

Clusters in both molecular beams are ionized by a resonant two-photon, one-color or two-color process. The two laser pulses are overlapped in time and space for the two-color ionization case. The lasers are two independent Nd/YAG pumped dye lasers. The output of these dye lasers is doubled or doubled and mixed as is appropriate for the excitation ($S_1 \leftarrow S_0$) and ionization ($I \leftarrow S_1$) transition. In a two-color ionization, the $S_1 \leftarrow S_0$ excitation laser is reduced in intensity to minimize the one-color contribution to the signal. Thus, the wavelength of the second (ionization, $I \leftarrow S_1$) laser could be scanned across the ionization threshold to open or close a particular ionization or reaction/fragmentation channel.

The ion beam is extracted into a TOF tube that is perpendicular to both the molecular and laser beams. At the end of the flight tube (1.5 m) ions of different mass are separated by their time-of-flight and are detected by a microchannel plate detector (operated at a gain of $\sim 10^7$) equipped with two microchannel plates in Chevron configuration. The output current from the detector is fed (at 50 Ω) into a Tektronix RTD 720A transient digitizer without additional amplification. The digitizer samples the ion detector voltage at a rate of 4 ns/channel; a trace of 8192 or 16 384 samples is acquired after each laser pulse (a scan), corresponding to a maximum TOF of 32 or 64 μ s. Between laser pulses (100 ms), the acquired scan or trace is transferred to a Gateway P6-180 MHz computer for real-time processing of the covariance matrix. The RTD 720A digitizer is chosen because of its data throughput over a GPIB port. Data transfer to the computer and processing one trace of 8192 samples takes less than 100 ms and one trace of 16 384 samples takes less than 200 ms. Data can thus be collected and processed at a laser repetition rate of 5 or 10 Hz.

IV. CALCULATION OF COVARIANCES AND CORRELATION COEFFICIENTS

Covariance matrix elements are calculated for each pair of peaks in a mass spectrum; for each laser pulse, ion signal intensities are integrated (typically 15–25 time samples) and each pair of integrated peaks is treated according to Eqs. (1) and (2). So obtained, covariances or correlation coefficients are presented in tabular form, a covariance or correlation coefficient matrix. The dimensions of these matrices range roughly from $5 \times 5 = 25$ elements to $20 \times 20 = 400$ elements. In the analysis approach used herein, ion intensities from two mass peaks (with widths a and b time samples) are first integrated and then integrated intensities are correlated. This procedure gives exactly the same result as one in which the steps are reversed: that is, each two time samples are correlated, and the resulting covariance intensities are integrated over the grid of $a \times b$ points. This follows from rearrangement of the summations in Eq. (1). The covariance and correlation coefficients are only weakly dependent on the cho-

sen integration interval, as is to be expected, as off-peak intensity is due mostly to unrelated background counts.

Through this integration procedure, information on any possible momentum correlation is lost because signals from both forward and backward scattered ions are added. This is only of minor concern for the present studies because we do not expect such associations for Eqs. (3)–(6). Importantly, however, by summing the signal intensities in each mass peak, a smaller number of scans is needed to achieve acceptable signal/noise ratios and error bars for measured covariances and correlation coefficients. For example, the typical cluster ion signal intensities in this study are about 10 ions/mass peak/laser pulse (~ 80 mV). The peak width varies with cluster size, but for many clusters of interest it is typically about 80 ns (100% width—full width at half-maximum ~ 25 ns). Since the peak shape is roughly Gaussian, on average about 1.4 ions will be detected in the time channel at the center of the mass peak. Typically 2500 scans are obtained for each single covariance matrix. Under these conditions the covariance values of the points spanning the area $a \times b$ in the map corresponding to two correlated mass peaks ($\sim 20 \times 20$ points) vary greatly; often neighboring points have opposite signs and a false impression may first arise that a positive correlation between some parts of the correlated peaks and a negative correlation between other parts of these peaks exists. Closer and more detailed consideration, however, reveals that randomness of the distribution of the covariance intensities within the chosen area is the cause for such behavior; that is, the variations are due solely to poor statistics. At the same time, correlation of the integrated ion signal intensities yields covariances with very reasonable and reproducible statistical deviations, typically $2\sigma = 0.04$ for correlation coefficients. For the Gaussian shaped peak under discussion, the statistical deviation of the covariance for the central time element of peaks would be seven times greater than that for the integrated peak intensity (area $a \times b$). About 1.75×10^4 scans would need to be collected to achieve acceptable error bars for the covariance at the central point of this area compared to 2.5×10^3 scans for the integrated peak areas.

Quoted errors for the covariances reported in these studies are 2σ corresponding to a 95% confidence level for each covariance matrix element in the map. Two different methods can be employed to obtain a reasonable estimate of the covariance matrix elements' standard deviation. In the first method, covariance is calculated according to Eq. (1) and statistical deviation of the covariance is calculated from the well-known expression for the statistical deviation of the mean:

$$\sigma = \sqrt{\frac{1}{n(n-1)} \sum_{i=1}^n [(x_i - \bar{x})(y_i - \bar{y}) - C(x,y)]^2}.$$

In the second method, the total number n of acquired samples is divided into m groups ($n/m \sim 100$), the covariance is calculated for each group separately, and the covariance and standard deviations are obtained as the mean and standard deviation of the mean for m observables.⁸ Correlation coefficients of course follow from these different ap-

TABLE I. $S_1 \leftarrow S_0$ excitation energies, apparent ionization energies (not corrected for a 300 V/cm electric field in the ion extraction region of the TOF mass spectrometer), and ion fragmentation threshold energies of TW_3 clusters.

| | $S_1 \leftarrow S_0$ transition energy (cm^{-1}) | Ionization energy (cm^{-1}) | Fragmentation threshold energy (cm^{-1}) |
|--|---|--|---|
| TW_3 | 37 606 | 70 075 | |
| $TW_3^+ \rightarrow W_3H^+ + C_6H_5CH_2$ | | | 70 940 |
| $TW_3^+ \rightarrow TW_2^+ + W$ | | | 71 855 |

proaches directly. The covariances calculated by both methods are equivalent within the stated error bars ($\pm 2\sigma$). In principle the first method, which includes all samples taken together, can suffer from low frequency error sources, while the second method omits these contributions. The results reported in this study are not subject to such differences.

V. TOLUENE/WATER CLUSTERS

A. Toluene(water) $_n$ ($n = 1, \dots, 6$)

The resonant two-photon ionization spectra of toluene(water) $_n$, $n = 1, \dots, 6$ (TW_n), have been studied previously.⁹ These clusters undergo extensive fragmentation subsequent to ionization, even if the energy of the ionizing photon is tuned only a few hundred cm^{-1} above the ionization threshold.

TW^+ and TW_2^+ cluster ions fragment by loss of a water molecule, while larger TW_n^+ ($n \geq 3$) cluster ions fragment in two channels: loss of water and loss of the benzyl radical. For TW_3^+ , loss of a benzyl radical is the lower energy (two-color ionization) fragmentation channel, yielding W_3H^+ cluster ions. At high ionization energy (e.g., one-color ionization), loss of a water molecule is the preferred fragmentation channel. Table I contains a summary of energy relationships for these two channels. Correlations between TW_3^+ , W_3H^+ , and TW_2^+ ion signals reflect the competition between these two channels. Tables II and III show correlation coefficient matrices obtained for two-color ($\sim 72\,000 \text{ cm}^{-1}$) and one-color (at $75\,200 \text{ cm}^{-1}$) ionization, respectively, for TW_3^+ pumped ($S_1 \leftarrow S_0$) at $37\,606 \text{ cm}^{-1}$. Under two-color ionization conditions, the TW_3^+ ion correlates most strongly with W_3H^+ and more weakly with TW_2^+ (see Table II). The third strongest correlation is between TW_2^+ and W_3H^+ . Notice that the correlations of all cluster mass peaks with the background mass peak (probably pump oil) are zero within the error bars, as should be anticipated.

Figure 1 illustrates why TW_3^+ and W_3H^+ are positively correlated. In the lower trace of Fig. 1 is displayed the conventional mass spectrum obtained as an average of 500 scans or laser pulses; the upper trace displays the mass spectrum from a single scan selected from the set of 500 scans to demonstrate this correlation between TW_3^+ and W_3H^+ . Notice the relative intensities of the features and especially that a large signal for TW_3^+ generates a large signal for W_3H^+ .

On the other hand, under one-color ionization conditions the situation is reversed; that is, TW_3^+ correlates most strongly with TW_2^+ and more weakly with W_3H^+ (see Table

TABLE II. Correlation coefficient (γ) matrix of toluene water clusters ionized by resonant two-photon, two-color near-threshold ionization.

| | W_3H^+ | W_4H^+ | TW^+ | TW_2^+ | TW_3^+ | T_2W^+ | Background ⁺ | $T_2W_2^+$ |
|-------------------------|----------|-------------------|-------------------|-------------------|-------------------|--------------------|-------------------------|-------------------|
| W_3H^+ | | 0.278 ± 0.066 | 0.293 ± 0.072 | 0.382 ± 0.068 | 0.607 ± 0.082 | 0.088 ± 0.184 | -0.095 ± 0.092 | 0.164 ± 0.074 |
| W_4H^+ | | | 0.142 ± 0.068 | 0.239 ± 0.066 | 0.294 ± 0.068 | 0.058 ± 0.042 | -0.068 ± 0.060 | 0.078 ± 0.064 |
| TW^+ | | | | 0.264 ± 0.066 | 0.292 ± 0.070 | 0.022 ± 0.0148 | -0.106 ± 0.082 | 0.032 ± 0.074 |
| TW_2^+ | | | | | 0.390 ± 0.070 | 0.053 ± 0.120 | -0.154 ± 0.074 | 0.061 ± 0.070 |
| TW_3^+ | | | | | | 0.075 ± 0.182 | -0.065 ± 0.092 | 0.190 ± 0.076 |
| T_2W^+ | | | | | | | -0.179 ± 0.412 | 0.007 ± 0.110 |
| Background ⁺ | | | | | | | | 0.233 ± 0.070 |

III). $\gamma(TW_2^+, W_3H^+)$, $\gamma(TW_2^+, TW^+)$, $\gamma(TW^+, W_3H^+)$, and $\gamma(TW_3^+, TW^+)$ are also quite strong. Thus, the correlation matrices are consistent with the switching between fragmentation channels with change in ionization energy: the fragmentation channel $TW_3^+ \rightarrow W_3H^+ + C_6H_5CH_2\cdot$ prevails under two-color conditions, while the $TW_3^+ \rightarrow TW_2^+ + W$ channel dominates under one-color conditions.

Moreover, Table III shows that under one-color ionization conditions, TW_3^+ undergoes fragmentation by loss of two water molecules, consistent with the earlier spectroscopic results.⁹ Some of the TW_n^+ ions are also formed by fragmentation of $T_2W_n^+$; that is, $C(T_2W_n^+, TW_n^+)$ is large.

B. (Toluene)_m(water)_n ($m > 1$, $n < 5$)

To test the covariance mapping technique further on a more complex fragmenting system, larger clusters of the toluene/water system have been studied: in particular, (toluene)_m(water)_n, ($m > 1$, and $n < 5$) clusters. To carry out this test of covariance mapping for a fragmenting system, the spectroscopy of these clusters must first be explored. The details of ionization, fragmentation channels, and the various spectra are given in Table IV. A few general remarks will be presented in the text here to orient the reader. First, the mass spectrum of $T_m W_n^+$ ($m > 1, n < 5$) cluster ions shows prominent even-odd alternation of cluster ion signal intensities with varying number n of water molecules; that is, $T_m W_2^+$ and $T_m W_4^+$ are more abundant in the mass spectrum than $T_m W_1^+$ and $T_m W_3^+$ (see Fig. 2). Second, the excitation spectra of $T_2 W_n^+$ ($n < 5$) clusters show sharp spectral features for $S_1 \leftarrow S_0$ of toluene in the vicinity of the toluene bare molecule $S_1 \leftarrow S_0$, superimposed on a broad absorption continuum (Fig. 3). Table IV presents the appropriate spectroscopic results and fragmentation energies for the clusters of present concern.

Again, information on the ionization threshold and fragmentation channels for a collection of clusters can be employed to observe correlation coefficients and covariance matrix elements as these thresholds are scanned. In particular, $\gamma(T_2 W_n^+, T_2 W_k^+)$ are characterized as the ionization laser energy is scanned from below to above the threshold for the $T_2 W_2^+ \rightarrow T_2 W^+ + W$ fragmentation channel. With the excitation laser at $37\,592\text{ cm}^{-1}$ both the $T_2 W_2$ cluster ($S_1 \leftarrow S_0$) specifically and a broad background absorption from other clusters ($T_m W_k, m > 1$) are accessed. The laser intensity is kept low, as described above for a two-color ionization, to reduce the one-color signal component. The ionization laser is scanned from $33\,445$ to $34\,700\text{ cm}^{-1}$.

As expected, $\gamma(T_2 W_2^+, T_2 W^+)$ increases as this fragmentation channel is scanned by the ionization laser; however, $\gamma(T_2 W_3^+, T_2 W^+)$ and $\gamma(T_2 W_4^+, T_2 W^+)$ also increase by about the same factor as $\gamma(T_2 W_2^+, T_2 W^+)$ does, while $\gamma(T_2 W_3^+, T_2 W_2^+)$, $\gamma(T_2 W_4^+, T_2 W_2^+)$, and $\gamma(T_2 W_4^+, T_2 W_3^+)$ remain unchanged (see Fig. 4). $T_2 W^+$ cannot correlate with $T_2 W_4^+$ and $T_2 W_3^+$ due to fragmentation under these excitation conditions (see Table IV). Thus, $T_2 W^+$ can be correlated with $T_2 W_3^+$ and $T_2 W_4^+$ only through cluster growth. The increase of $\gamma(T_2 W_3^+, T_2 W^+)$ and $\gamma(T_2 W_4^+, T_2 W^+)$ with the opening of the $T_2 W_2^+ \rightarrow T_2 W^+ + W$ fragmentation channel is then solely due to the increase of the $T_2 W^+$ ion signal intensity. This observation demonstrates that the correlation coefficients depend on signal intensities and that covariances in general are not well normalized through division by $\sqrt{\sigma^2(x)\sigma^2(y)} \equiv \sqrt{C(x,x)C(y,y)}$.

Surprisingly, this possibility has thus far been ignored in the literature. In Sec. VI, we present a simple model to explore this circumstance. Below we discuss two issues: (1) separation of the two contributions (growth and fragmentation) to correlation coefficients through the observed ionization laser intensity and wavelength dependence of the corre-

TABLE III. Correlation coefficient (γ) matrix of toluene water clusters ionized by resonant two-photon, one-color ionization.

| | W_3H^+ | W_4H^+ | TW^+ | TW_2^+ | TW_3^+ | T_2W^+ | $T_2W_2^+$ |
|----------|----------|-------------------|-------------------|-------------------|-------------------|-------------------|-------------------|
| W_3H^+ | | 0.112 ± 0.068 | 0.213 ± 0.072 | 0.274 ± 0.066 | 0.182 ± 0.068 | 0.168 ± 0.066 | 0.098 ± 0.066 |
| W_4H^+ | | | 0.094 ± 0.064 | 0.135 ± 0.066 | 0.096 ± 0.066 | 0.060 ± 0.062 | 0.033 ± 0.062 |
| TW^+ | | | | 0.271 ± 0.064 | 0.169 ± 0.064 | 0.238 ± 0.068 | 0.088 ± 0.064 |
| TW_2^+ | | | | | 0.272 ± 0.070 | 0.189 ± 0.066 | 0.113 ± 0.056 |
| TW_3^+ | | | | | | 0.120 ± 0.062 | 0.153 ± 0.060 |
| T_2W^+ | | | | | | | 0.128 ± 0.062 |

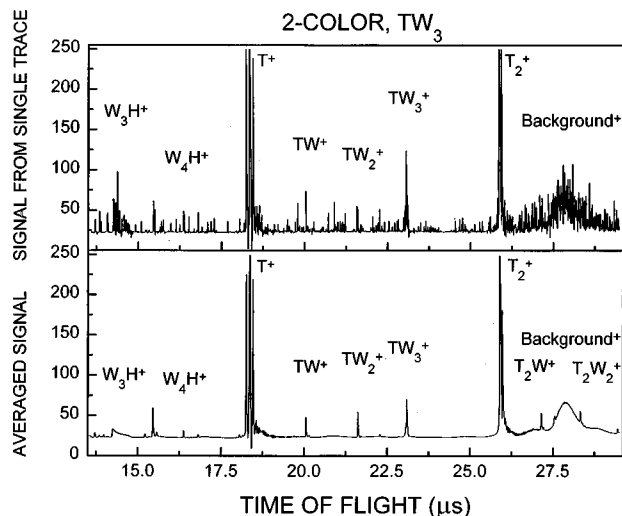


FIG. 1. Lower trace: The mass spectrum of the TW_n^+ ($n < 5$) and $T_2W_n^+$ ($n < 3$) cluster ions produced by resonant two-photon, two-color ionization, obtained as an average of 500 scans. Upper trace: The mass spectrum from a single individual scan selected from the set of 500 scans. The excitation (one-photon) energy is tuned to $TW_3 S_1 \leftarrow S_0$ resonance at $37\,606\text{ cm}^{-1}$. The ionization energy is $\sim 34\,480\text{ cm}^{-1}$. The corresponding correlation coefficient matrix is shown in Table II.

lation coefficients; and (2) proper normalization of the covariance to eliminate this signal (or laser) intensity dependence.

VI. CORRELATIONS DUE TO NEUTRAL CLUSTER GROWTH AND CLUSTER ION FRAGMENTATION BASED ON THEIR LASER INTENSITY DEPENDENCE—A SIMPLE MODEL

As seen in Fig. 5, the reason that the correlation coefficients are not independent of ionization laser intensity or the signal product intensity for the two correlated ions is that $C(x^+, y^+)$ scales as $I(\text{laser})^n$, $n = 1.8 \pm 0.2$, and $[\sigma(x)\sigma(y)]$ scales as I_L^m , $m = 1.2 \pm 0.1$ (I_L is the ionization laser intensity). Thus, $\gamma(x^+, y^+) = C(x^+, y^+)/\sigma(x)\sigma(y)$ scales as I_L^l , $l = 0.6 \pm 0.2$. Note, of course, that $[x][y]$ (=signal product intensity for x^+ and y^+ ion signals) scales as I_L^2 .

The specific question is now: why is the signal dependence of covariance matrix elements $C([T_2W_n^+], [T_2W_k^+])$ steeper than that of the variance matrix elements

TABLE IV. $S_1 \leftarrow S_0$ excitation energies, apparent ionization energies (not corrected for a 300 V/cm electric field in the ion extraction region of the TOF mass spectrometer), and ion fragmentation threshold energies of T_2W_n , $1 \leq n \leq 4$, clusters.

| | $S_1 \leftarrow S_0$ transition energy (cm^{-1}) | Ionization energy (cm^{-1}) | Fragmentation threshold energy (cm^{-1}) |
|-------------------------------------|---|--|---|
| T_2W | 37 459.5 | $69\,790 \pm 100$ | |
| T_2W_2 | 37 592 | $69\,690 \pm 100$ | |
| $T_2W_2^+ \rightarrow T_2W^+ + W$ | | | $71\,290 \pm 200$ |
| T_2W_3 | 37 558.5 | $69\,310 \pm 150$ | |
| $T_2W_3^+ \rightarrow T_2W_2^+ + W$ | | | $72\,060 \pm 200$ |
| T_2W_4 | 37 547 | $68\,260 \pm 150$ | |
| $T_2W_4^+ \rightarrow T_2W_3^+ + W$ | | | $72\,060 \pm 200$ |

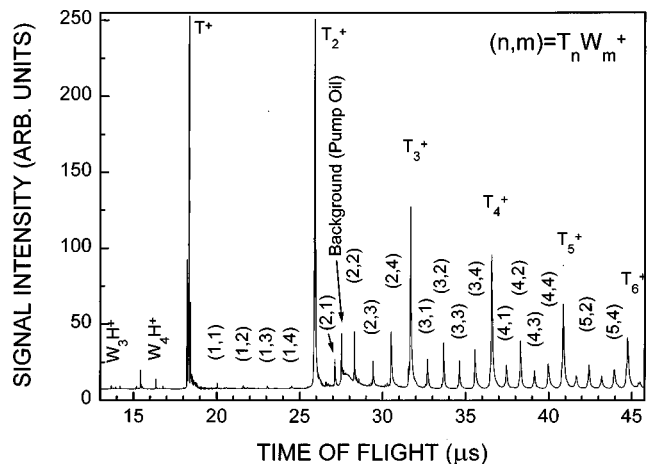


FIG. 2. The mass spectrum of the $T_mW_n^+$ ($n < 5$) cluster ions produced by resonant two-photon, one-color ionization. Notice prominent even-odd alternations of signal intensity with number of water molecules n for $m > 1$. The excitation (one-photon) energy ($37\,584\text{ cm}^{-1}$) is tuned to the broad background absorption of T_mW_n ($m > 1$) clusters, off any TW_n or T_2W_n resonance.

$C([T_2W_n^+], [T_2W_k^+]) = \sigma^2(T_2W_n^+)$ and $\sigma^2(T_2W_k^+) = C([T_2W_k^+], [T_2W_k^+])$? The short answer to this question, which we will sketch below in terms of a simple model, is that different fluctuations Δ may contribute to the covariance and variance matrix elements.

Consider the sequence of neutral cluster growth, cluster ionization, and cluster ion fragmentation reactions [Eqs. (3)–(6)] described in Sec. II. For convenience these equations are written in a simple diagram as

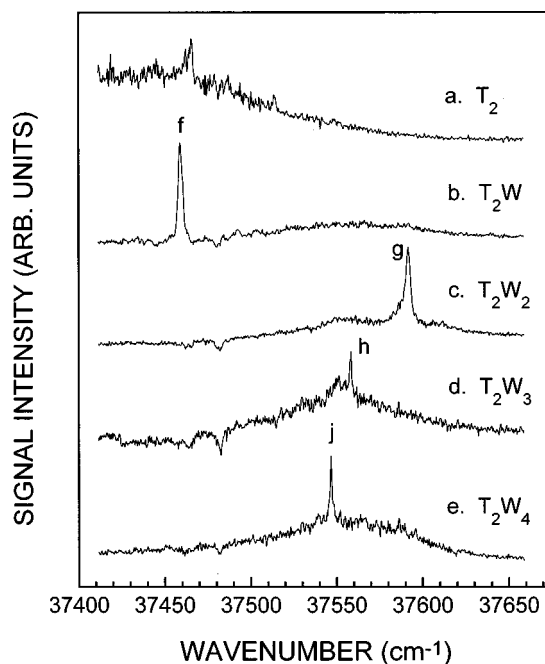


FIG. 3. Two-color mass resolved excitation spectra of T_2W_n clusters: (a) toluene₂, (b) toluene₂(H₂O)₁, (c) toluene₂(H₂O)₂, (d) toluene₂(H₂O)₃, and (e) toluene₂(H₂O)₄.

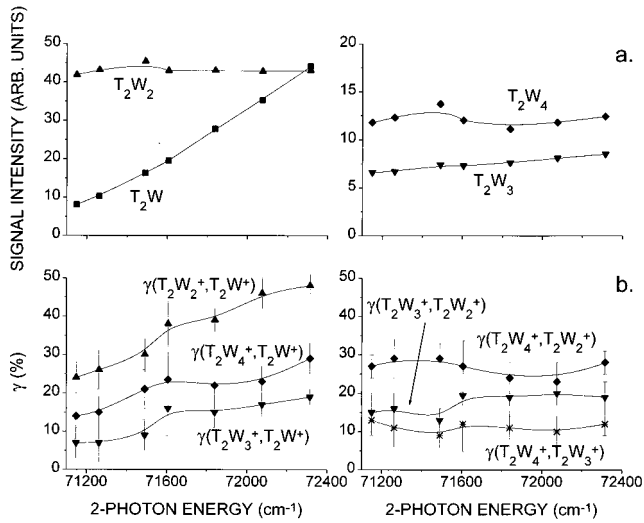
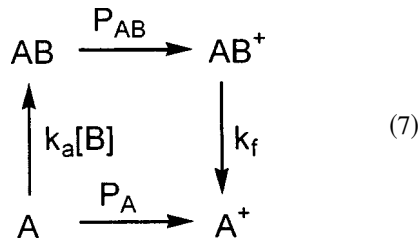


FIG. 4. (a) $T_2W_n^+$ ($n < 5$) ion signal intensities and (b) $\gamma(T_2W_n^+, T_2W_k^+)$ correlation coefficients as functions of the two-photon energy obtained by scanning the ionization laser photon energy across the threshold for the $T_2W_2^+ \rightarrow T_2W^+ + W$ fragmentation channel ($\sim 71\,290\text{ cm}^{-1}$). The excitation energy is $37\,592\text{ cm}^{-1}$.



Here, $k_a[B]$ denotes the cluster growth or aggregation rate, P_A , P_{AB} , are ionization probabilities, and k_f is the fragmentation rate of cluster ion AB^+ . To simplify the mathematics of the model and reduce the complexity of the final formulas, consider a simple model for cluster growth and fragmentation that will nevertheless take into account all the important kinetics in the reaction sequence Eq. (7) above affecting correlations. This model is based on the following assumptions: (1) A particles are monomers; (2) exponential kinetic formulas can be approximated by the leading linear terms in their Taylor series expansions; (3) cluster growth rate $k_a[B]$ is given in units of growth probability/unit time the cluster spends in the molecular beam; (4) fragmentation rate k_f is given in units of fragmentation probability/unit time the cluster ion spends in the ion source of the mass spectrometer; and (5) concentration dilution with increasing distance from the nozzle is the same for all species in the molecular beam. Then concentrations $[A]$ and $[AB]$ of particles A and AB at the end of the growth phase are related to the initial concentration $[A]_0$ of particle A before growth by

$$[A] = (1 - k_a[B])[A]_0, \quad (8)$$

$$[AB] = k_a[B][A]_0. \quad (9)$$

For cluster ions,

$$[A^+] = P_A[A] + k_f P_{AB}[AB], \quad (10)$$

$$[AB^+] = (1 - k_f)P_{AB}[AB]. \quad (11)$$

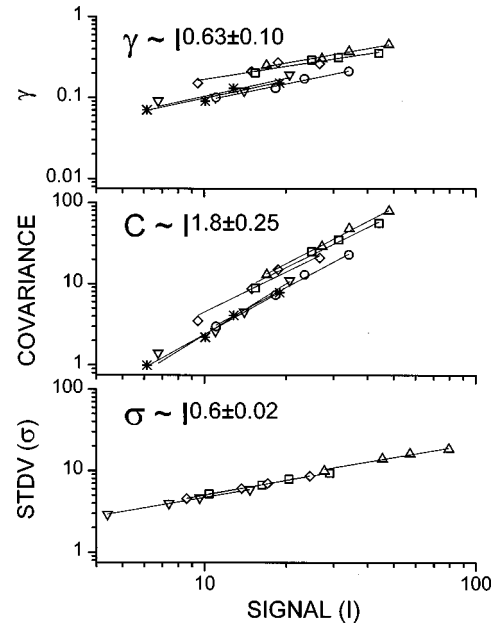


FIG. 5. Dependencies of (a) correlation coefficients $\gamma(T_2W_n^+, T_2W_k^+)$ and (b) covariances $C(T_2W_n^+, T_2W_k^+)$ on the geometric average I of the signal intensities $I(T_2W_n^+)$ and $I(T_2W_k^+)$, $I = \sqrt{I(T_2W_n^+) \cdot I(T_2W_k^+)}$; \triangle — $n=2$, $k=1$; ∇ — $n=3$, $k=1$; \diamond — $n=4$, $k=1$; \circ — $n=3$, $k=2$; \square — $n=4$, $k=2$; and $*$ — $n=4$, $k=3$. (c) Dependencies of the standard deviations $\sigma(T_2W_n^+) = \sqrt{C(T_2W_n^+, T_2W_n^+)}$ on the signal intensities $I(T_2W_n^+)$: \square — $n=1$; \triangle — $n=2$; ∇ — $n=3$; and \diamond — $n=4$. The signal intensities I are varied by varying the ionization laser intensity I_L , $I \propto I_L$.

Combining these formulas, the ion concentrations can be written as

$$[A^+] = (P_A(1 - k_a[B]) + k_f P_{AB} k_a[B])[A]_0, \quad (12)$$

$$[AB^+] = (1 - k_f)P_{AB} k_a[B][A]_0. \quad (13)$$

Measured ion signals are proportional to ion concentrations so the signals can be taken as the ion concentrations without loss of generality. The covariance $C([A^+], [AB^+])$ can then be expressed as the mean of the product of ion signal deviations,

$$\begin{aligned}
 C([A^+], [AB^+]) &= \frac{1}{n} \sum_{i=1}^n (\Delta[A^+]_i \Delta[AB^+]_i) \\
 &= \langle \Delta[A^+] \Delta[AB^+] \rangle
 \end{aligned}$$

with

$$\Delta[A^+]_i = [A^+]_i - \langle [A^+] \rangle,$$

$$\Delta[AB^+]_i = [AB^+]_i - \langle [AB^+] \rangle, \quad (14)$$

$$\langle [X^+] \rangle = \frac{1}{n} \sum_{i=1}^n [X^+]_i.$$

The ion signal deviations $\Delta[A^+]$ and $\Delta[AB^+]$ can be obtained by differentiating Eqs. (12) and (13), respectively. The algebra is tedious but straightforward. A number of fluctuation terms in this expression are zero. Denote the mean of the product of two fluctuations $\Delta\alpha$ and $\Delta\beta$ as $\langle \Delta\alpha \Delta\beta \rangle$. If these fluctuations are independent, $\langle \Delta\alpha \Delta\beta \rangle = 0$.

For example, $\langle \Delta[A]_0 \Delta P_A \rangle = \langle \Delta[A]_0 \Delta P_{AB} \rangle = \langle \Delta[A]_0 \Delta k_f \rangle = \langle \Delta k_a[B] \Delta P_A \rangle = \langle \Delta k_a[B] \Delta P_{AB} \rangle = \langle \Delta k_a[B] \Delta k_f \rangle = 0$. Nozzle fluctuations can leave $\langle \Delta[A]_0 \Delta k_a[B] \rangle$ nonzero and laser fluctuations can leave $\langle \Delta P_A \Delta P_{AB} \rangle$ nonzero.

$\langle \Delta P_A \Delta k_f \rangle$ and $\langle \Delta P_{AB} \Delta k_f \rangle$ will be zero because the number of absorbed photons by each cluster does not change with laser fluctuations. The covariance between $[A^+]$ and $[AB^+]$ is then given by

$$\begin{aligned}
C([A^+], [AB^+]) &= (P_A(1 - k_a[B]) + k_f P_{AB} k_a[B])(1 - k_f) P_{AB} k_a[B] \langle (\Delta[A]_0)^2 \rangle \\
&\quad - (P_A - k_f P_{AB})(1 - k_f) P_{AB} [A]_0^2 \langle (\Delta k_a[B])^2 \rangle \\
&\quad + (1 - k_f) P_{AB} (k_a[B](-P_A + P_{AB} k_f) + P_A(1 - k_a[B]) + k_f P_{AB} k_a[B]) [A]_0 \langle \Delta k_a[B] \Delta[A]_0 \rangle \\
&\quad + (1 - k_a[B])(1 - k_f) k_a[B] [A]_0^2 \langle \Delta P_A \Delta P_{AB} \rangle \\
&\quad + k_f (k_a[B])^2 (1 - k_f) [A]_0^2 \langle (\Delta P_{AB})^2 \rangle \\
&\quad - P_{AB}^2 (k_a[B])^2 [A]_0^2 \langle (\Delta k_f)^2 \rangle.
\end{aligned} \tag{15}$$

The first three terms on the right-hand side of Eq. (15) are growth related, the fourth term is laser intensity fluctuation dependent, and the last two terms are fragmentation related. Note that if ions A^+ and AB^+ are not coupled by fragmentation ($k_f=0$), the last two terms are zero. The fourth term is nonzero only if laser intensity fluctuations are significant.

The first four terms of Eq. (15) scale with (laser intensity, I_L).² Terms 1, 2, and 3 are proportional to $(P_A P_{AB})$ or $(P_{AB} P_{AB})$ times products of correlated fluctuations that occur prior to ionization. The ionization probabilities scale with I_L and thus the dependence on laser intensity of these three terms follows. Therefore, these growth terms scale with I_L^2 . The fourth term in Eq. (15) is proportional to $\langle \Delta P_A \Delta P_{AB} \rangle$ times factors not dependent on laser power. The only correlations between P_A and P_{AB} are laser fluctuation induced, and thus $\langle \Delta P_A \Delta P_{AB} \rangle \propto \langle \Delta I_L^2 \rangle$; $\langle \Delta I_L^2 \rangle \propto \langle I_L^2 \rangle$. Terms 1–4 of Eq. (15) scale with I_L^2 . Term 5 is proportional to $\langle (\Delta P_{AB})^2 \rangle$ and terms independent of laser power. The scaling of this term with laser intensity depends on the nature of the ΔP_{AB} fluctuations: if laser fluctuations dominate $\langle (\Delta P_{AB})^2 \rangle \propto \langle (\Delta I_L)^2 \rangle \propto I_L^2$, if Poisson ion count fluctuations dominate $\langle (\Delta P_{AB})^2 \rangle \propto [AB^+] \propto I_L$.

Normal laser pulse intensity variations are $\sim 8\%$ and selected pulses can be as low as $3\%–5\%$. No change in the signal behavior or correlation coefficients is observed upon pulse selection, and thus laser power fluctuations are not dominant contributions to our results. Thus term 5 in Eq. (15) should scale as I_L .

Term 6 in Eq. (15) is proportional to P_{AB}^2 times fluctuations of the fragmentation probability $\langle (\Delta k_f)^2 \rangle$. In these experiments k_f fluctuates due only to the statistical nature of the fragmentation process, and this fluctuation will depend on the number of ions: $P_{AB}^2 \langle (\Delta k_f)^2 \rangle$ will thus scale with I_L .

In summary, covariance terms due to cluster fragmentation [terms 5 and 6 in Eq. (15)] scale linearly with laser intensity, and covariance terms due to cluster growth [terms 1, 2, and 3 in Eq. (15)] scale quadratically with laser intensity. Laser intensity fluctuations [term 4 in Eq. (15)] are only small contributors to the covariance in our experiments and can be further de-emphasized through laser pulse selection.

Thus cluster growth ($\propto I_L^2$) and cluster fragmentation ($\propto I_L$) contributions to the covariance map matrix elements can be determined through the laser intensity dependence of the covariance.

Expressions for the variances or diagonal covariance matrix elements, $C([A^+], [A^+])$ and $C([AB^+], [AB^+])$ can also be generated. The variances differ from the covariances in one major way: fluctuations of the ionization probability contribute to the $C(x^+, x^+)$ and $C(y^+, y^+)$ in the form $\langle (\Delta P_x)^2 \rangle$ and $\langle (\Delta P_y)^2 \rangle$ but not $\langle (\Delta P_x \Delta P_y) \rangle$. This difference clearly is expressed by the fourth term in Eq. (15). These contributions are now present even if the fragmentation contribution k_f is small or zero. ΔP_A and ΔP_{AB} result from the statistical nature of the ionization processes and the small number (~ 10) of ions/mass peak, so the expected Poisson fluctuations are $\sim 30\%$ in the ion signal (as observed). Thus ΔP_A and ΔP_{AB} are the prevailing fluctuations for the variances, while the growth terms are the prevailing fluctuation source for the covariances. Hence, the signal variances, $C([A^+], [A^+]) = \sigma^2([A^+])$ and $C([AB^+], [AB^+]) = \sigma^2([AB^+])$, will scale as signal or laser intensity. This is the reason that the neutral cluster growth dominated $\gamma([A^+], [AB^+]) = C([A^+], [AB^+]) / \sigma([A^+]) \sigma([AB^+])$ does not become signal intensity independent as should be expected. $\gamma([A^+], [AB^+])$ still scales as the laser intensity because covariances are growth (I_L^2) dominated and variances are ion fluctuation dominated (I_L).

VII. APPLICATION OF MODELING RESULTS TO THE FRAGMENTATION OF $T_2W_n^+$ CLUSTER IONS

Figure 5 shows that the covariances $C([T_2W_n^+], [T_2W_k^+])$ ($n, k=1–4$) scale with the power $1.6–2$ of $([T_2W_n^+][T_2W_k^+])^{1/2}$. In these experiments $[x^+] \propto I_L$ and thus the covariances $C([x^+], [y^+]) \propto I_L^{1.6–2.0}$. Figure 6 gives a linear plot for the covariances and a fit to the relation

$$\begin{aligned}
C([T_2W_n^+], [T_2W_k^+]) &= A([T_2W_n^+][T_2W_k^+])^{1/2} \\
&\quad + B\{([T_2W_n^+][T_2W_k^+])^{1/2}\}^2.
\end{aligned}$$

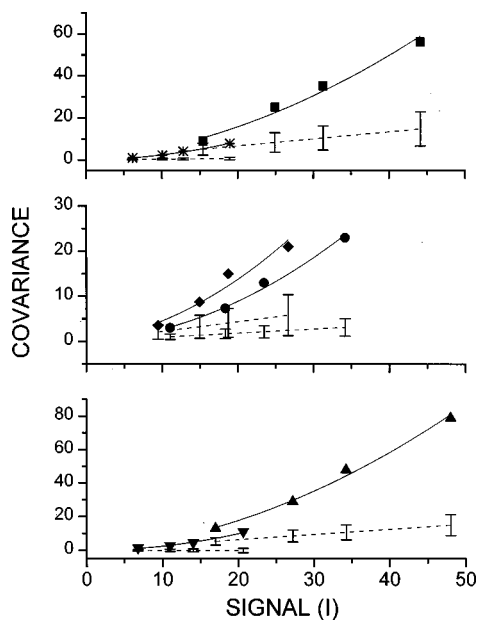


FIG. 6. Solid lines: Dependencies of covariances $C(T_2W_n^+, T_2W_k^+)$ on the geometric average I of the signal intensities $I(T_2W_n^+)$ and $I(T_2W_k^+)$, $I = \sqrt{I(T_2W_n^+) \cdot I(T_2W_k^+)}$ from Fig. 5 plotted on linear scale. Dashed lines: Linear signal intensity dependence components A of the covariances obtained by fitting $C(T_2W_n^+, T_2W_k^+) = AI + BI^2$. The uncertainty of the least-squares fits are indicated by error bars: \blacktriangle — $C(T_2W_2^+, T_2W^+)$ $= (0.31 \pm 0.13)I + (0.029 \pm 0.004)I^2$. \blacktriangledown — $C(T_2W_3^+, T_2W^+)$ $= (-0.01 \pm 0.06)I + (0.025 \pm 0.004)I^2$. \blacklozenge — $C(T_2W_4^+, T_2W^+)$ $= (0.22 \pm 0.17)I + (0.023 \pm 0.009)I^2$. \bullet — $C(T_2W_3^+, T_2W_2^+)$ $= (0.09 \pm 0.06)I + (0.017 \pm 0.002)I^2$. \blacksquare — $C(T_2W_4^+, T_2W_2^+)$ $= (0.33 \pm 0.18)I + (0.023 \pm 0.006)I^2$. *— $C(T_2W_4^+, T_2W_3^+)$ $= (0.03 \pm 0.03)I + (0.020 \pm 0.002)I^2$.

The term linear in $([T_2W_n^+][T_2W_k^+])^{1/2}$ signifies covariance contributions due to cluster ion fragmentation, and the quadratic term signifies contributions due to neutral cluster growth. The main conclusion to be drawn from these data is that the contribution to the covariance matrix elements measured is mainly due to cluster growth and not cluster fragmentation. In principle, the fragmentation and growth components each could be quantified separately by this procedure; however, more experimental data points would be needed to reduce the fitting ambiguity.

An algebraic approach could also be employed to retrieve the small fragmentation component $C_f([x^+]_{\lambda_1}, [y^+]_{\lambda_1})$ of the total covariance $C([x^+]_{\lambda_1}, [y^+]_{\lambda_1})$ matrix element (measured at λ_1 ionization wavelength) in the presence of a large growth component for the measured covariance. If $C([x^+]_{\lambda_0}, [y^+]_{\lambda_0})$ is the covariance measured at λ_0 below the fragmentation threshold so that $C([x^+]_{\lambda_0}, [y^+]_{\lambda_0}) = C_a([x^+]_{\lambda_0}, [y^+]_{\lambda_0})$ the growth contribution, then $\{C([x^+]_{\lambda_1}, [y^+]_{\lambda_1}) - C_a([x^+]_{\lambda_0}, [y^+]_{\lambda_0})\}$ should be equal to $C_f([x^+]_{\lambda_1}, [y^+]_{\lambda_1})$. Since the covariance depends on signal intensity, however, the $C_a([x^+]_{\lambda_0}, [y^+]_{\lambda_0})$ must be corrected for the actual signal intensities at λ_1 ($[x^+]_{\lambda_1}$ and $[y^+]_{\lambda_1}$) before the subtraction can be made to obtain $C_f([x^+]_{\lambda_1}, [y^+]_{\lambda_1})$. The algebra to do this is tedious but straightforward.

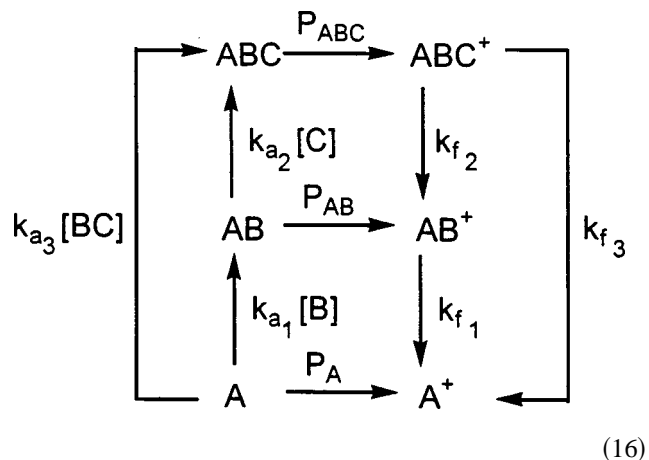
Below the fragmentation threshold $C_f([x^+], [y^+]) = 0$. If laser fluctuations are small ($<5\%$ as selected), then

$C_a([x^+], [y^+])$ depends on λ through the product of the signal intensities, and $C_a([x^+]_{\lambda_1}, [y^+]_{\lambda_1})$ is related to $C_a([x^+]_{\lambda_0}, [y^+]_{\lambda_0})$ through the ratio of the signal intensity products at λ_1 and λ_0 . The subtraction can then be made and $C_f([x^+]_{\lambda_1}, [y^+]_{\lambda_1})$ can be determined. Specifically,

$$C_f([x^+]_{\lambda_1}, [y^+]_{\lambda_1}) = \left(C([x^+]_{\lambda_1}, [y^+]_{\lambda_1}) - \left(\frac{[x^+]_{\lambda_1}[y^+]_{\lambda_1}}{[x^+]_{\lambda_0}[y^+]_{\lambda_0}} \right) C([x^+]_{\lambda_0}, [y^+]_{\lambda_0}) \right)$$

As discussed in Sec. V, the correlation coefficients $\gamma([T_2W_n^+], [T_2W_k^+])$ ($n, k = 1, \dots, 4$) and corresponding covariances $C([T_2W_n^+], [T_2W_k^+])$ are measured as functions of the ionization photon wavelength (λ_1). The wavelength of the ionization laser λ is scanned across the fragmentation threshold for the $T_2W_2^+ \rightarrow T_2W^+ + W$ fragmentation channel (see Fig. 4). Using the above approach, the $C_f([T_2W_n^+], [T_2W_k^+])$ covariance matrix elements are determined for $|n - k| = 1$. For $n = 2, k = 1$, the results are quite similar to those obtained by the plotting technique discussed above: $\gamma_f([T_2W_2^+], [T_2W^+]) \sim 10 \pm 5\%$ (see Fig. 7) and $\gamma([T_2W_2^+], [T_2W^+]) \sim 45\%$ (see Fig. 4). That is, the fragmentation contribution to the total covariance is small for this system.

To determine the fragmentation components $C_f([T_2W_3^+], [T_2W^+])$ and $C_f([T_2W_4^+], [T_2W_k^+])$, the signal intensity dependence of $C_a([T_2W_3^+], [T_2W^+])$ and $C_a([T_2W_4^+], [T_2W_k^+])$ must be estimated. To do so, the model must be expanded somewhat to include sequential and/or parallel cluster growth reactions. The reaction diagram for $T_2W_3^+$ ions, for example, consistent with experimental observations is



in which $A = T_2W$, $B = C = W$, and $BC = W_2$. Assuming that $\Delta k_{a_1}[B]$ and $\Delta k_{a_2}[C]$ are small compared to $\Delta[A]_0$ or $\Delta k_{a_3}[BC]$, one can apply the same reasoning given above to extract the appropriate covariances. Two situations can arise for which this approach holds: cluster growth fluctuations occur at the early stages of growth; and $T_2W + W_2 \rightarrow T_2W_3$. Note that if $k_{f_2} = k_{f_3} = 0$, $C([A^+], [ABC^+])$ would be caused entirely by cluster growth. Figure 7 displays these results for $\gamma_f([T_2W_n^+], [T_2W_k^+])$. Note that

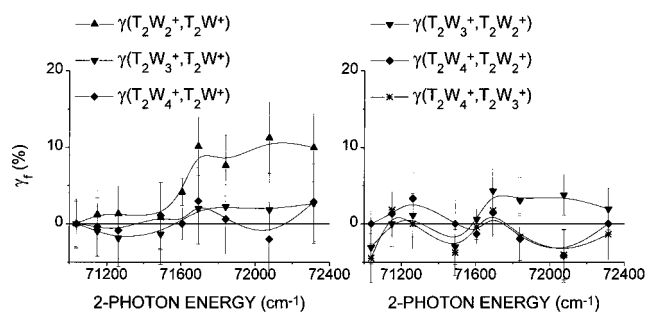


FIG. 7. Ion fragmentation components of the correlation coefficients, $\gamma_f(T_2W_n^+, T_2W_k^+)$, as functions of the two-photon energy obtained by scanning the ionization laser photon energy across the threshold for the $T_2W_2^+ \rightarrow T_2W^+ + W$ fragmentation channel. Note that $\gamma_f(T_2W_2^+, T_2W^+)$ increases as the fragmentation channel opens while $\gamma_f(T_2W_n^+, T_2W_k^+)$ ($n \neq 2, k \neq 1$) are zero within the error bars, as should be expected.

$\gamma_f([T_2W_n^+], [T_2W_k^+])$ is nonzero only for $n=2, k=1$, consistent with $T_2W_2^+ \rightarrow T_2W^+ + W$ being the only open fragmentation channel.

We have demonstrated that the covariance matrix elements and correlation coefficient $C([T_2W_n^+], [T_2W_k^+])$ and $\gamma([T_2W_n^+], [T_2W_k^+])$ are dominated by terms that scale as $I_L^2 \propto ([T_2W_n^+], [T_2W_k^+])$ and that these terms must be related to cluster growth. The question now arises: why are the fragmentation contributions to the correlation coefficients and covariance matrix elements so small when the T_2W^+ ion current increases by a factor of 5 due to fragmentation? Note that the reaction discussed earlier, $TW_3^+ \rightarrow W_3H^+ + \text{benzyl}$, is not growth dominated for obvious reasons and the covariance $C([TW_3^+], [W_3H^+])$ does reveal fragmentation behavior as different fragmentation channels are opened.

We have argued in Sec. I that fluctuations due to cluster fragmentation should be higher than those from cluster growth and that correlations due to fragmentation should, in general, be expected to be higher than those due to cluster growth. Nonetheless, data show that for the $T_mW_n^+$ system, cluster growth contributions dominate the covariance. One possible explanation for this behavior is that formation of stable $T_2W_2^+$ ions and formation of the unstable $T_2W_2^+$

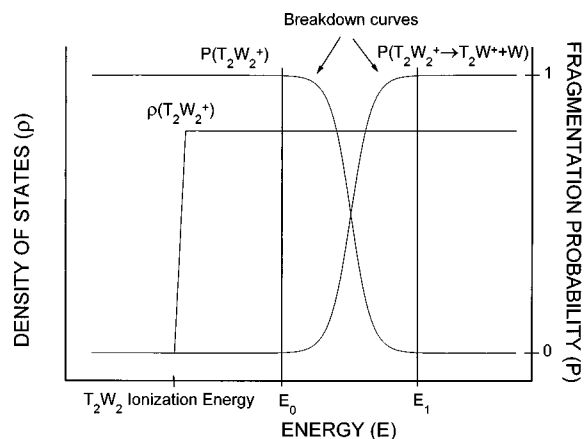


FIG. 8. Schematic diagram showing dependencies of the density of states of $T_2W_2^+$ [$\rho(T_2W_2^+)$] and the probabilities of $T_2W_2^+$ to remain intact [$P(T_2W_2^+)$] or to fragment [$P(T_2W_2^+ \rightarrow T_2W^+ + W)$] (breakdown curves) as functions of cluster ion energy.

($\rightarrow T_2W^+ + W$) ions are independent of one another and thus uncorrelated, except for a very narrow range of energies. Figure 8 displays dependencies of the density of states of $T_2W_2^+$ and the probabilities of $T_2W_2^+$ either to remain intact or to fragment as functions of cluster ion energy (breakdown curves). Consider these ion energy ranges: $E < E_0$, in which $T_2W_2^+$ does not fragment; $E_1 > E > E_0$, in which $T_2W_2^+$ may or may not fragment, and $E > E_1$, in which $T_2W_2^+$ will fragment with high probability. The probability to populate a particular ion state depends on the properties of the final state but is independent of ionization photon energy (as long as the photon energy is higher than the energy of this ion state). The density of states in these three regions is assumed constant and the number of ions produced within a given energy range is simply proportional to the number of states with energies lower than the photon energy. Ions falling in the range $E_1 > E > E_0$ will contribute to the covariance $C([T_2W_2^+], [T_2W^+])$; whether or not ions in the ranges $E < E_0$ and $E > E_1$ will contribute to $C([T_2W_2^+], [T_2W^+])$ depends on ionization efficiency. If the ionization efficiency of T_2W_2 is small, then no correlation will exist for these two groups and $C([T_2W_2^+], [T_2W])$ will not be affected by these ions; if, on the other hand, the ionization efficiency is large so that most T_2W_2 are ionized, then one ion population will be generated at the expense of the other. $C([T_2W_2^+], [T_2W^+])$ will be affected by this contribution and the covariance would be negative if this contribution were dominant. Since this latter possibility is not observed, we must conclude that the ionization cross section for these clusters is small. Thus $\gamma_f([T_2W_2^+], [T_2W^+])$ is small because (1) the difference ($E_1 - E_0$) is small ($\sim 400 \text{ cm}^{-1}$) and (2) the ionization efficiency is low for this system. Fluctuations in $[T_2W^+]$ and $[T_2W_2^+]$ signals thereby contribute to the variances, $\sigma^2[T_2W^+]$ and $\sigma^2[T_2W_2^+]$, but not the covariances $C([T_2W_2^+], [T_2W^+])$. This mechanism is consistent with the step behavior of $\gamma_f([T_2W_2^+], [T_2W^+])$ and its constancy following the step in the $\langle E_0, E_1 \rangle$ region.

Fragmentation thresholds are often not known for a system and the covariance cannot always be measured below these thresholds. In such instances, the two components (growth and fragmentation) contributing to cluster ion correlations may not always be separable; nevertheless, the idea that the $C([A^+], [AB^+])$ varies with the product of signal intensities $[A^+][AB^+] \propto I_L^2$ suggests the following definition of a normalized covariance $\bar{C}([x^+], [y^+])$:

$$\bar{C}([x^+], [y^+]) = \frac{C([x^+], [y^+])}{[x^+][y^+]}. \quad (17)$$

As shown above, this normalization of the covariance removes the major source of laser intensity dependence of the covariance due to the cluster growth component. Note that $\bar{C}([x^+], [y^+])$ is different from $\gamma([x^+], [y^+])$ as the correlation coefficient relates the product of correlated fluctuations to the product of all (correlated and uncorrelated) fluctuations through the variances $C([x^+], [x^+])$ and $C([y^+], [y^+])$. $\gamma([A^+], [AB^+])$ removes the laser and signal intensity dependence for fragmentation dominated covariance, whereas $\bar{C}([A^+], [AB^+])$ removes this dependence for growth dominated covariance.

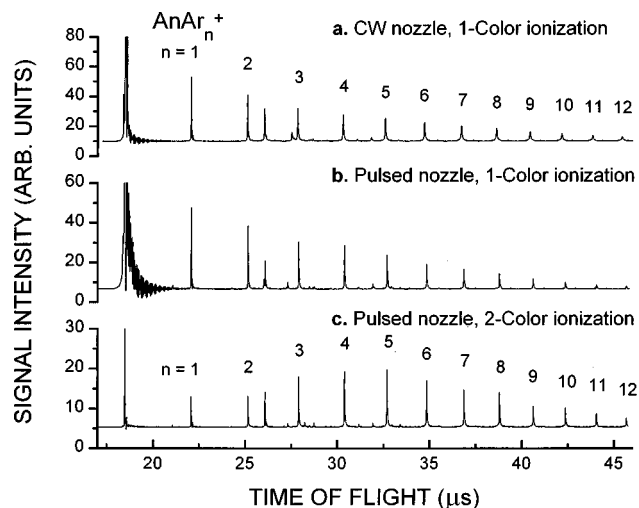


FIG. 9. The mass spectra of the AnAr_n^+ cluster ions obtained from different supersonic nozzles and under different ionization conditions: (a) continuous-flow nozzle, one-color ionization; (b) pulsed nozzle, one-color ionization; and (c) pulsed nozzle, two-color (near-threshold) ionization. The corresponding normalized covariance matrices are shown in Tables V(b), V(a), and VI, respectively.

VIII. CLUSTER GROWTH DYNAMICS OF ANILINE/ARGON AND 4-FLUOROSTYRENE/ARGON

These two cluster systems are chosen for study because neutral cluster growth is found to be the dominant contribution for the covariance mapping of the toluene/water system. The argon clusters of aniline (An) and 4-fluorostyrene (FS) should present a simplified picture and one through which the growth terms in the covariance matrix can be more carefully and more thoroughly probed. Both Knight and co-workers¹⁰ and Bréchnignac and co-workers^{11–13} have done detailed energy, simulation, and cluster studies of these systems.

In spite of the strong similarities in the structures and stabilities of AnAr_n and FSAr_n clusters, their apparent one-color mass spectra are quite different. AnAr_n^+ cluster ion intensity in a mass spectrum steadily decreases with increasing cluster size n , while the FSAr_n^+ cluster ion intensity has a number of local maxima at $n = 4, 8, 20$, with the most intense feature in the spectrum at $n \sim 4, 8, \text{ or } 20$ depending on expansion conditions. This difference in cluster distribution behavior for AnAr_n and FSAr_n is suggested to be due to cluster fragmentation. One-color, two-photon ionization of FSAr_n essentially creates ions in their ground vibrational states with little excess energy, while the same conditions for AnAr_n creates ions with as much as 6000 cm^{-1} of excess energy. We study these two systems because this suggested difference should be readily measurable with the covariance mapping analysis presented above and should lend more weight to it.

A. Aniline/Ar clusters

The mass spectrum of AnAr_n^+ cluster ions ionized by a one-color, two-photon process through the $\text{An } S_1 \leftarrow S_0$ is shown in Fig. 9. Spectra from pulsed and continuous nozzles are essentially identical. As reported previously,⁷ the cluster ion intensity decreases with increasing cluster size n .

The normalized covariances $\bar{C}([\text{AnAr}_k^+], [\text{AnAr}_n^+])$, $n, k = 1, \dots, 12$, for both expansions are given in Table V. The \bar{C} values are different for both the experiments, but the pattern is the same: The normalized covariances are independent of cluster size. For the pulsed nozzle, $\bar{C}([\text{AnAr}_n^+], [\text{AnAr}_k^+]) \sim 0.025 \pm 0.010$ and for the cw nozzle $\bar{C}([\text{AnAr}_n^+], [\text{AnAr}_k^+]) \sim 0.070 \pm 0.010$. Clearly these correlations are not dependent on pulse-to-pulse nozzle fluctuations. The normalized covariance matrix elements, as described in Sec. VII, are employed here to present the AnAr_n correlation data because the covariance matrix elements are again shown to scale with the signal intensity product of the two ions involved in the correlation.

The careful two-color, two-photon ionization spectrum of AnAr_n clusters with excess energy at AnAr of $\sim 500 \text{ cm}^{-1}$ and about 1100 cm^{-1} at AnAr_5 is shown in Fig. 9, as well. The intensity distribution of mass peaks is different than that found in the one-color ionization spectrum and the difference is, of course, due to the nearly complete elimination of cluster ion fragmentation. This distribution peaks at about $n \sim 5$ but the signals are quite weak due to the required low intensity of the excitation laser beam ($\sim 20 \text{ μJ/pulse}$). The ionization beam energy is $\sim 2 \text{ mJ/pulse}$ in this instance. The appearance of the spectrum notwithstanding, the normalized covariance matrix elements (see Table VI) are nearly identical to those presented above and are constant throughout the covariance map. This should not be surprising as, for the system parameters appropriate for van der Waals clusters, growth behavior is the major contributor to the covariance. Fragmentation due to the one-color AnAr_n ionization is rapid (according to RRK¹⁴ estimates) and dominates the appearance of the ensuing cluster ion mass distribution.

What can be concluded about cluster growth dynamics from the observation that $\bar{C}([\text{AnAr}_n^+], [\text{AnAr}_k^+])$ are independent of cluster size n and k ? Using a simplified probabilities model for cluster growth, one can demonstrate that fluctuations of argon concentration in the beam and fluctuations of the cluster growth rate coefficients have a cumulative effect; that is, the number of fluctuation contributions to $\bar{C}([\text{AnAr}_n^+], [\text{AnAr}_k^+])$ grows with cluster size n and k . Since the measured $\bar{C}([\text{AnAr}_n^+], [\text{AnAr}_k^+])$ are almost independent of cluster size and n and k , the contribution to the fluctuations as cluster size grows must be negligible. This suggests that the fluctuations related to reactions $\text{AnAr}_i + \text{Ar} \rightarrow \text{AnAr}_{i+1}$, $i \geq 1$, are small. Moreover, fluctuations of ionization probabilities $\Delta P_n \Delta P_k$ are correlated only through laser intensity fluctuation. These terms are shown to be small by laser pulse selection. The normalized covariances are thus dependent most importantly on terms of the form

$$\frac{\langle \{\Delta(k_{0 \rightarrow 1}[\text{An}][\text{Ar}])\}^2 \rangle}{(k_{0 \rightarrow 1}[\text{An}][\text{Ar}])^2}$$

with $k_{0 \rightarrow 1}$ being the rate coefficient for the formation of the AnAr cluster (“dimer”). Thus, the measured $\bar{C}([\text{AnAr}_n^+], [\text{AnAr}_k^+])$ are consistent with a model in which the dominant fluctuations occur at the first step of the cluster growth sequence and propagate to clusters of larger sizes as aggregates grow by argon condensation on AnAr . The dimer

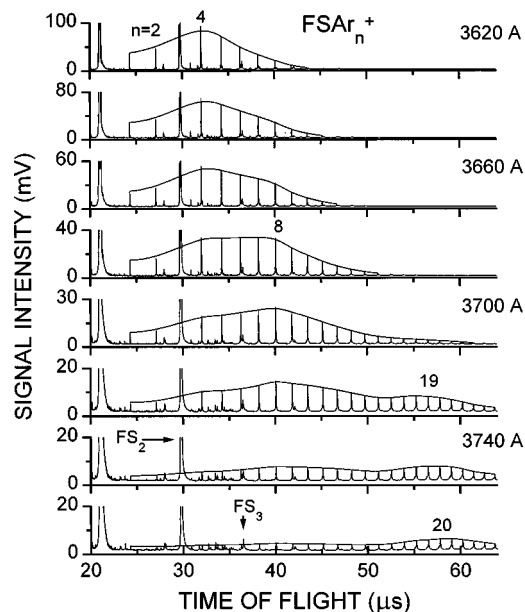


FIG. 10. The mass spectra of the FSAr_n^+ cluster ions obtained for different pulsed nozzle currents. Note that increasing the nozzle current leads to larger effective nozzle opening area and longer opening time. The effect is similar to increasing the backing gas pressure, i.e., the cluster distribution shifts to larger cluster size. Note the multinodal character of the FSAr_n^+ cluster size distribution. To guide the eyes, the FSAr_n^+ peak intensity maxima have been fitted by B -spline curves.

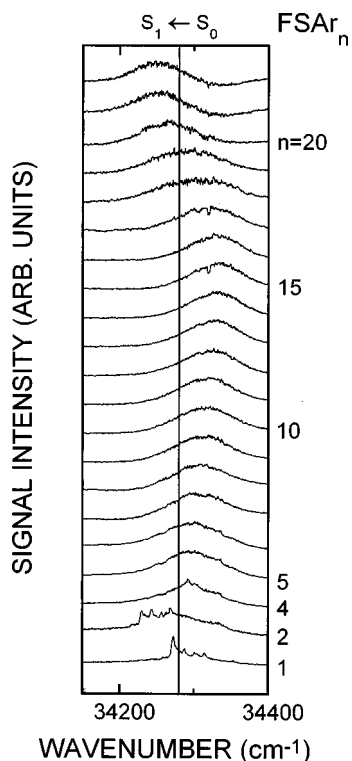


FIG. 11. The mass resolved excitation spectra of FSAr_n^+ , $n=1,2,4,\dots,22$ clusters. Note a small progressive blueshift of the $S_1 \leftarrow S_0$ absorption for $n \leq 15$ followed by larger progressive redshift for $n > 15$. The solid vertical line indicates the excitation wave number ($34\,282\text{ cm}^{-1}$) used to record the FSAr_n^+ mass spectra.

TABLE VII. Signal intensity correction factors for FSAr_n^+ cluster ions accounting for cluster size variations of the $S_1 \leftarrow S_0$ photoabsorption cross section at excitation energy of $34\,282\text{ cm}^{-1}$.

| FSAr_n | Correction |
|--------------------|------------|
| FSAr_4 | 0.960 |
| FSAr_5 | 0.997 |
| FSAr_6 | 1.045 |
| FSAr_7 | 0.994 |
| FSAr_8 | 1.028 |
| FSAr_9 | 1.078 |
| FSAr_{10} | 1.182 |
| FSAr_{11} | 1.248 |
| FSAr_{12} | 1.428 |
| FSAr_{13} | 1.541 |
| FSAr_{14} | 1.630 |
| FSAr_{15} | 1.707 |
| FSAr_{16} | 1.768 |
| FSAr_{17} | 1.248 |
| FSAr_{18} | 1.117 |
| FSAr_{19} | 0.993 |
| FSAr_{20} | 0.942 |
| FSAr_{21} | 1.163 |
| FSAr_{22} | 1.276 |

measured by Bréchnac *et al.*¹² but are somewhat less resolved because we use 100% Ar rather than 5% Ar in He as the expansion gas in order to observe larger clusters). The spectra for clusters with $n > 4$ are reported for the first time in this work. They show an interesting cluster size trend. The $S_1 \leftarrow S_0$ absorption exhibits a small progressive blueshift with increasing cluster size for $n \leq 15$ followed by a larger progressive redshift for $n > 15$. The vertical solid line in Fig. 11 indicates the wavelength ($34\,282\text{ cm}^{-1}$) used to record the mass spectra shown in Fig. 10. Table VII lists ratios of the absorption band areas integrated between $34\,150$ and $34\,400\text{ cm}^{-1}$ to absorption at $34\,282\text{ cm}^{-1}$. The mass spectral intensities can be multiplied by these correction factors to correct the mass spectra with respect to the varying absorption cross section. Correction factors for $n < 10$ are quite small, which suggests that the cluster ion distribution peaks at $n \sim 4$ and 8 are not due to photoabsorption cross section variations but are characteristic of the neutral cluster distribution. The corrected mass distribution is quite flat between cluster sizes 10 and 20 (Fig. 12). Such a flat distribution is probably a result of superposition of two distribution maxima; therefore we tentatively suggest that there exists a third maximum in the neutral distribution peaking at $n \sim 20$, but the existence of this node is less certain than that of those at $n \sim 4$ and 8 .

The clear impression these spectra give is that larger clusters grow at the expense of smaller ones: the $n \sim 4$ local maximum decreases as the $n \sim 8$ local maximum develops, etc. (see Fig. 10). Compared to the AnAr_n cluster distribution for two-color, two-photon near threshold ionization, the FSAr_n distribution is similar but seems to develop more maxima and to form larger clusters more readily.

Covariance mapping techniques can be employed here to uncover more information concerning the origins of the observed multinodal character of the FSAr_n^+ mass distribution. The covariance matrix for this system is tabulated in Table

TABLE IX. Simulated normalized covariance (\bar{C}) matrix of FSAr_n^+ cluster ions corresponding to the cluster size distribution displayed in Fig. 13. For details of the simulation see the text. Note that the extraordinarily high value of $\bar{C}(\text{FSAr}_2^+, \text{FSAr}^+)$ is a simulation artifact [arising when the parameter j (see the text) is allowed to reach too small values], and should be ignored.

| | FSAr^+ | FSAr_2^+ | FSAr_3^+ | FSAr_4^+ | FSAr_5^+ | FSAr_6^+ | FSAr_7^+ | FSAr_8^+ | FSAr_9^+ | FSAr_{10}^+ | FSAr_{11}^+ | FSAr_{12}^+ | FSAr_{13}^+ |
|----------------------|-----------------|-------------------|-------------------|-------------------|-------------------|-------------------|-------------------|-------------------|-------------------|----------------------|----------------------|----------------------|----------------------|
| FSAr^+ | | 0.707 | 0.076 | -0.042 | -0.104 | -0.138 | -0.149 | -0.150 | -0.150 | -0.156 | -0.170 | -0.195 | -0.237 |
| FSAr_2^+ | | | 0.141 | 0.032 | -0.017 | -0.045 | -0.057 | -0.059 | -0.059 | -0.060 | -0.064 | -0.072 | -0.086 |
| FSAr_3^+ | | | | 0.039 | 0.009 | -0.012 | -0.024 | -0.028 | -0.030 | -0.032 | -0.035 | -0.041 | -0.049 |
| FSAr_4^+ | | | | | 0.016 | 0.002 | -0.008 | -0.014 | -0.017 | -0.019 | -0.022 | -0.026 | -0.033 |
| FSAr_5^+ | | | | | | 0.010 | 0.003 | -0.002 | -0.005 | -0.008 | -0.011 | -0.014 | -0.019 |
| FSAr_6^+ | | | | | | | 0.011 | 0.008 | 0.005 | 0.003 | 0.001 | -0.001 | -0.004 |
| FSAr_7^+ | | | | | | | | 0.013 | 0.012 | 0.011 | 0.010 | 0.010 | 0.009 |
| FSAr_8^+ | | | | | | | | | 0.015 | 0.016 | 0.016 | 0.017 | 0.019 |
| FSAr_9^+ | | | | | | | | | | 0.019 | 0.020 | 0.023 | 0.027 |
| FSAr_{10}^+ | | | | | | | | | | | 0.024 | 0.028 | 0.035 |
| FSAr_{11}^+ | | | | | | | | | | | | 0.035 | 0.044 |
| FSAr_{12}^+ | | | | | | | | | | | | | 0.057 |

which will yield the proper normalized covariance matrix elements. A good qualitative fit can be achieved within the following approximation scheme.

First, fit the measured average FSAr_n mass spectrum with a linear combination of two log-normal distributions $A(n)$ and $B(n)$. This implies that the monomer aggregation probability increases with some power of the cluster size. The position of the distributions $A(n)$ and $B(n)$ maxima are at $n=4$ and 8, respectively. All other parameters are varied in the least-squares fitting program. Figure 13 shows the measured cluster intensities, the best fit $x_1A(n) + x_2B(n)$, the individual distributions $x_1A(n)$ and $x_2B(n)$, and the normalized distributions $A(n)$ and $B(n)$ both of which have the same area.

Second, fluctuations are chosen to have the form $yA'(n) - yB'(n)$ with y generated randomly from a normal distribution with $\sigma \sim 0.1x_1$. Distributions $A'(n)$ and $B'(n)$ have exactly the same shape as $A(n)$ and $B(n)$, but the positions of their maxima j and k are allowed to fluctuate from cluster sizes $n=4$ and $n=8$, respectively, with fluctuations $j-4$ and $k-8$ generated randomly from a normal distribution with $\sigma=2$.

The covariance matrix is computed from 2500 data records. For each data record a new set of parameters y, j, k , is generated by a random number generator and the cluster distribution is calculated by the formula

$$I(n) = x_1A(n) + yA'(n) + x_2B(n) - yB'(n). \quad (18)$$

The calculated covariance matrix is presented in Table IX. The agreement between the experimental results in Table VIII and those calculated with the simple model is quite reasonable. Clearly the trend of covariance values across or down Table IX is like that in Table VIII. This fit suggests that FSAr_n clusters grow in the manner modeled: A cluster distribution at low n value (~ 4) quickly forms and then larger nodal patterns ($n \sim 8, \sim 20$) develop at the expense of the smaller one(s). The shuffling of cluster intensity from one mode peaking at $n=4$ to the next mode peaking at $n=8$ is simulated here by varying parameter y from positive to negative values. Note that the covariance matrix elements are very sensitive to this growth behavior while the averaged mass spectrum of FSAr_n is not. The absolute values in the

simulated covariance table (Table IX) are lower than those in the measured covariance table (Table VIII). This difference may be attributed to the oversimplification of the modeling scheme, e.g., we assume that the total number of clusters formed does not vary from pulse to pulse. Table X contains comparable results for an experiment at higher pressures of Ar such that the distribution of FSAr_n has these local maxima at $n \sim 8, 20$.

Apparently each local maximum in the multinodal FSAr_n^+ cluster ion size distribution results from a different set of growth kinetic parameters. The FSAr_n distribution shape is different than that found for AnAr_n . The FSAr_n distribution is very sensitive to small random changes of the parameters in the supersonic expansion; these fluctuations shuffle intensity from one distribution node to another. A kinetic model presented in Sec. IX will show that this case is consistent with fast kinetic rates for both the FSAr (dimer) formation and for the formation of larger FSAr_n clusters. FSAr dimers must form rapidly while the density of Ar is still high in the molecular jet so that further cluster distribution patterns ($n \sim 4 \rightarrow n \sim 8 \rightarrow n \sim 19$) can develop. Because the growth kinetics are fast, small changes in Ar concentration have rather profound effects on the cluster distribution.

The reason the FSAr_n cluster distribution changes discontinuously ($n \sim 4 \rightarrow n \sim 8 \rightarrow \sim 19$) rather than smoothly is probably associated with cluster stability relations, associated with the decrease of cluster growth rate upon closing of solvation shells or half shells.

IX. SIMULATION OF CLUSTER GROWTH KINETICS

The covariance data suggest that cluster growth kinetics of FSAr_n clusters are faster than those of AnAr_n clusters. To elucidate which of the cluster growth parameters (dimer formation rate, cross-section-size dependence, overall rates, concentrations, etc.) might be responsible for this difference, a simple numerical model is developed to simulate cluster growth and its dependence on argon concentration, the AnAr (or FSAr) dimer formation rate, and the rates of subsequent steps in the growth process. In the equations below R stands for either the FS or An chromophore. The kinetics of RAR_n formation can be characterized by the rate equations,

TABLE X. Normalized covariance (\bar{C}) matrix of FSAr_n^+ cluster ions produced at high pulsed valve currents. For sake of brevity, all normalized covariances are multiplied by a factor of 1000. The standard deviations (2σ) of the normalized covariances are between ± 0.004 (for values smaller than 0.050) and ± 0.012 (for values larger than 0.050). The corresponding mass spectrum cluster size distribution is shown in Fig. 12.

| n/n | 4 | 5 | 6 | 7 | 8 | 9 | 10 | 11 | 12 | 13 | 14 | 15 | 16 | 17 | 18 | 19 | 20 | 21 | 22 | 23 | 24 | 25 |
|-------|---|----|----|----|----|----|----|----|----|----|----|----|----|----|-----|-----|-----|-----|-----|-----|-----|-----|
| 4 | | 52 | 52 | 53 | 51 | 47 | 42 | 38 | 31 | 24 | 19 | 12 | 4 | -3 | -7 | -11 | -14 | -18 | -23 | -23 | -23 | -23 |
| 5 | | | 52 | 54 | 51 | 47 | 43 | 38 | 32 | 25 | 19 | 13 | 6 | -1 | -6 | -10 | -13 | -17 | -20 | -22 | -23 | -22 |
| 6 | | | | 54 | 53 | 49 | 44 | 38 | 33 | 25 | 20 | 11 | 3 | -5 | -10 | -15 | -18 | -23 | -28 | -29 | -30 | -30 |
| 7 | | | | | 54 | 49 | 45 | 40 | 34 | 27 | 21 | 13 | 4 | -3 | -8 | -13 | -16 | -22 | -26 | -27 | -28 | -29 |
| 8 | | | | | | 49 | 44 | 39 | 34 | 26 | 21 | 12 | 3 | -4 | -10 | -15 | -19 | -24 | -30 | -30 | -31 | -32 |
| 9 | | | | | | | 43 | 39 | 33 | 27 | 22 | 14 | 5 | -3 | -8 | -13 | -17 | -22 | -27 | -29 | -30 | -31 |
| 10 | | | | | | | | 37 | 33 | 27 | 23 | 16 | 9 | 1 | -4 | -8 | -13 | -17 | -23 | -24 | -26 | -28 |
| 11 | | | | | | | | | 31 | 27 | 23 | 18 | 11 | 5 | 0 | -5 | -9 | -13 | -18 | -20 | -22 | -25 |
| 12 | | | | | | | | | | 27 | 24 | 20 | 15 | 9 | 5 | 1 | -2 | -7 | -12 | -14 | -16 | -19 |
| 13 | | | | | | | | | | | 25 | 23 | 19 | 16 | 14 | 10 | 8 | 3 | 0 | -4 | -5 | -8 |
| 14 | | | | | | | | | | | | 25 | 23 | 21 | 20 | 17 | 16 | 13 | 8 | 6 | 2 | 0 |
| 15 | | | | | | | | | | | | | 27 | 28 | 29 | 27 | 26 | 25 | 22 | 19 | 16 | 13 |
| 16 | | | | | | | | | | | | | | 36 | 40 | 40 | 41 | 41 | 39 | 36 | 33 | 31 |
| 17 | | | | | | | | | | | | | | | 50 | 54 | 56 | 57 | 58 | 55 | 53 | 51 |
| 18 | | | | | | | | | | | | | | | | 63 | 66 | 70 | 72 | 70 | 69 | 67 |
| 19 | | | | | | | | | | | | | | | | | 75 | 80 | 85 | 83 | 83 | 82 |
| 20 | | | | | | | | | | | | | | | | | | 88 | 94 | 94 | 93 | 94 |
| 21 | | | | | | | | | | | | | | | | | | | 106 | 106 | 108 | 110 |
| 22 | | | | | | | | | | | | | | | | | | | | 118 | 120 | 125 |
| 23 | | | | | | | | | | | | | | | | | | | | | 126 | 132 |
| 24 | | | | | | | | | | | | | | | | | | | | | | 138 |

$$\frac{d\langle \text{RAR}_n \rangle}{dt} = k_{(n-1) \rightarrow n} [\text{Ar}] \langle \text{RAR}_{n-1} \rangle - k_{n \rightarrow (n+1)} [\text{Ar}] \langle \text{RAR}_n \rangle, \quad n \geq 1 \quad (19)$$

in which $[\text{Ar}]$ is the concentration of argon, and $\langle \text{RAR}_k \rangle$ is the total flux of RAR_k clusters at time t in the expansion. The rate constants k_i are a function of buffer gas concentration ($[\text{Bg}] = \text{Ar}$ or He) in the beam. $k_{n \rightarrow (n+1)}$ can be expressed as

$$k_{n \rightarrow (n+1)} = ka_n \frac{ks_{n+1} [\text{Bg}] \tau_{n+1}}{1 + ks_{n+1} [\text{Bg}] \tau_{n+1}} \quad (20)$$

in which ka_n is the bimolecular collision rate of RAR_n with Ar to form the activated complex RAR_{n+1}^* , ks_{n+1} is the collision rate of RAR_{n+1}^* with buffer gas, $[\text{Bg}]$ is the buffer gas concentration, and τ_{n+1} is the lifetime of the activated complex. The lifetime τ_{n+1} increases rapidly with cluster size n due to the increase in internal degrees of freedom. For $n > 1$ the mean cluster lifetime is greater than the mean time between collisions with the buffer gas; that is, $ks_n [\text{Bg}] \tau_n \gg 1$. Under this assumption $k_{n \rightarrow (n+1)} = ka_n$ for $n \geq 1$. Assuming that this bimolecular collision rate ka_n increases with cluster size, ka can take the form $ka_n = k(n+1)^z$; z is one of the simulation input parameters.

τ_1 is much shorter than all other τ_n because the dimer has only three degrees of freedom for rigid R and atom Ar. Hence in the early stages of the expansion (the growth process), $ks_1 [\text{Bg}] \tau_1 < 1$ and $k_{0 \rightarrow 1} < ka_0 = k$. The ratio $k_{0 \rightarrow 1} / k$ will be the second input parameter in the simulation. The relative rate of dimer formation to further cluster growth can thereby be explored for its effect on covariances and cluster distributions. $k_{0 \rightarrow 1}$ (the dimer formation rate constant) will also decrease with distance from the nozzle (time of expansion) because of the decrease in $[\text{Bg}]$, but we will ignore this

factor for this simple simulation. This overestimates dimer formation in the later stages of the expansion. Additionally, the assumption is made that

$$[\text{Ar}] = \frac{[\text{Ar}]_0 \alpha d^2}{x^2} \sim \frac{[\text{Ar}]_0 \alpha d^2}{v^2 t^2}$$

for d the nozzle diameter, $\alpha = \alpha(C_p, C_v)$ (see Ref. 15), x the downstream distance from the nozzle, and v the beam velocity ($\sim 1 \times 10^5$ cm/s), and t time. Then

$$k_{n \rightarrow (n+1)} [\text{Ar}] = \frac{K_n}{t^2}$$

with

$$K_n = k_{n \rightarrow (n+1)} \frac{[\text{Ar}]_0 \alpha d^2}{v^2}, \quad (21)$$

$$\frac{d\langle \text{RAR}_n \rangle}{dt} = \frac{K_{n-1}}{t^2} \langle \text{RAR}_{n-1} \rangle - \frac{K_n}{t^2} \langle \text{RAR}_n \rangle.$$

This system of differential equations [Eq. (21)] can be solved in analytical form. With $\langle \text{RAR}_n \rangle(t_0) = 0$, the solution is

$$\langle \text{RAR}_n \rangle = \langle \text{R} \rangle_0 \prod_{i=0}^{n-1} K_i \sum_{i=0}^n \frac{\exp[K_i(1/t - 1/t_0)]}{\prod_{\substack{j=0 \\ j \neq i}}^n (K_j - K_i)}. \quad (22)$$

In Eq. (22) $\langle \text{R} \rangle_0$ is the flux of R (An or FS) from the nozzle, t_0 is the time at which the temperature of the beam is low enough for clustering to start, and the flux $\langle \text{RAR}_n \rangle$ of RAR_n clusters is calculated at time $t > t_0$ during the expansion. The final distribution at the end of the expansion is obtained for $1/t = 0$,

$$\langle RAr_n \rangle = \langle R \rangle_0 \prod_{i=0}^{n-1} K_i \sum_{i=0}^n \frac{\exp[-K_i/t_0]}{n \prod_{\substack{j=0 \\ j \neq i}} (K_j - K_i)}. \quad (23)$$

Using $k_{n \rightarrow (n+1)} = k(n+1)^z$, $n \geq 1$, we can express K_n , $n \geq 1$, in the form

$$K_n = K(n+1)^z \quad \text{with} \quad K = k \frac{[Ar]_0 a d^2}{v^2}. \quad (24)$$

The parameter K_0 describing dimer formation can be expressed as $K_0 = (k_{0 \rightarrow 1}/k)K$. The final computational form is

$$\begin{aligned} \frac{\langle RAr_n \rangle}{\langle R \rangle_0} = & \frac{k_{0 \rightarrow 1}}{k} \prod_{i=1}^{n-1} (i+1)^z \left[\frac{\exp\left(-\frac{k_{0 \rightarrow 1}}{k} K/t_0\right)}{\prod_{j=1}^n \left((j+1)^z - \frac{k_{0 \rightarrow 1}}{k}\right)} \right. \\ & \left. + \sum_{i=1}^n \frac{\exp[-(i+1)^z K/t_0]}{\left(\frac{k_{0 \rightarrow 1}}{k} - (i+1)^z\right) \prod_{\substack{j=1 \\ j \neq i}}^n [(j+1)^z - (i+1)^z]} \right]. \quad (25) \end{aligned}$$

In this latter equation the cluster distribution is expressed as a function of three dimensionless parameters: z , $k_{0 \rightarrow 1}/k$, and K/t_0 . The z parameter models the change in cross section for Ar addition to RAr_n as a function of cluster size n for $n \geq 1$. The parameter $k_{0 \rightarrow 1}/k$ expresses the rate of dimer formation relative to the clustering rates of larger clusters. The parameter K/t_0 describes the absolute size of the clustering rate. The first two parameters, z and $k_{0 \rightarrow 1}/k$, are characteristic of the system studied. K/t_0 scales with $[Ar]_0$ in the nozzle, with nozzle area, and with inverse time $1/t_0$. K/t_0 can model changes in backing pressure and pulsed nozzle current and the clustering rate constants K_n for $n > 1$.

In order to compare the experimental and simulated mass spectra distribution for $AnAr_n^+$ and $FSAr_n^+$ clusters, careful experimental intensities must be generated for both systems under exactly the same experimental conditions (e.g., timing, spatial distribution, laser powers, threshold ionization, etc.). Additionally, the parameters K/t_0 , $k_{0 \rightarrow 1}/k$, and z for both $AnAr_n^+$ and $FSAr_n^+$ clusters must also be compared to determined relative neutral cluster growth behavior for the two cluster systems. The (two-color) $AnAr_n$ and (one-color) $FSAr_n$ mass intensity distributions are determined simultaneously (by coexpanding aniline and 4-fluorostyrene in Ar) to ensure that experimental expansion conditions are identical. The observed $FSAr_n^+$ distributions are corrected for absorption cross sections as described in Sec. VIII B. This procedure is not necessary for $AnAr_n$ clusters for $2 < n < 15$. Figure 14 shows data for two different pulsed nozzle currents (equivalent to two different cw nozzle backing pressures p_1 and p_2 , $p_2 \sim 1.4p_1$).

For the simulated fit to these results for $AnAr_n^+$ and $FSAr_n^+$ distributions the three parameters of the fit are varied as follows: $z = 1/2$, and K/t_0 and $k_{0 \rightarrow 1}/k$ are varied to fit the

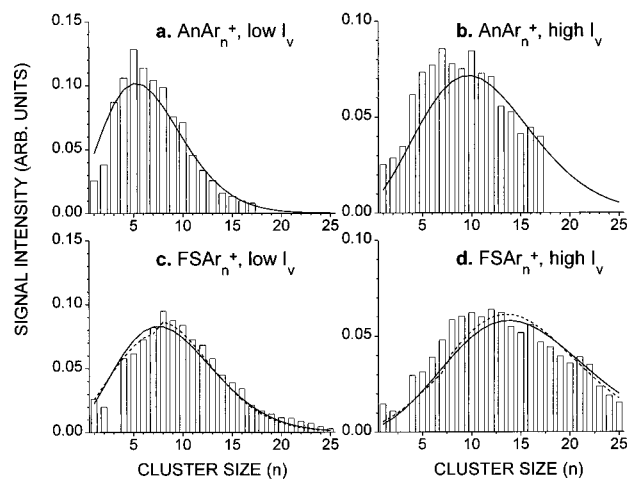


FIG. 14. The corrected measured (hollow bars) and simulated (solid and dashed lines) distributions of the $AnAr_n^+$ and $FSAr_n^+$ cluster ions produced by expanding simultaneously aniline and 4-fluorostyrene from the nozzle: (a) $AnAr_n^+$, low nozzle current; (b) $AnAr_n^+$, high nozzle current; (c) $FSAr_n^+$, low nozzle current; and (d) $FSAr_n^+$, high nozzle current. Note that at the same current the $FSAr_n^+$ distribution peaks at larger cluster size than the $AnAr_n^+$ distribution. The simulated distributions are obtained by fitting simultaneously the low and the high current distributions with one set of parameters. The dashed lines show fit of the $FSAr_n^+$ distributions when the cluster growth rates $K_{n \rightarrow n+1}$ for $n \geq 8$ are lowered by 10%, which would be consistent with solvation shell or half-shell closing at cluster size $n = 8$ (for details of the modeling and fitting procedures and results, see the text).

low current (pressure) distributions, and 1.4 K/t_0 and $k_{0 \rightarrow 1}/k$ are varied to fit the high current (pressure) distributions simultaneously. The best fit for $FSAr_n^+$ clusters is found for $K/t_0 = 4.6 \pm 0.3$ and $k_{0 \rightarrow 1}/k = 0.85 \pm 0.15$ (see Fig. 14) and the best fit for $AnAr_n^+$ clusters is found for $K/t_0 = 3.75 \pm 0.25$ and $k_{0 \rightarrow 1}/k = 0.85 \pm 0.15$. Thus both the dimer formation rate $k_{0 \rightarrow 1}$ and the overall cluster formation rate $K(\propto k)$ are faster (by roughly 25%) for neutral $FSAr_n$ cluster growth than for neutral $AnAr_n$ cluster growth. If the relative dimer formation rate constant $k_{0 \rightarrow 1}/k$ is too small (~ 0.1), a Poisson distribution of clusters is never achieved for any overall clustering rate K/t_0 , and the cluster intensity decreases with cluster size n .

The faster derived growth kinetics for $FSAr_n$ neutral clusters is consistent with both the observed pressure dependence of the distributions and the $FSAr_n^+$ covariance map matrix elements. The faster growth kinetics imply that small fluctuations of the parameters in supersonic expansion (i.e., the $[Ar]$ concentration, temperature, etc.) will lead to relatively larger cluster distribution changes on a pulse-to-pulse basis. This is consistent with the higher normalized covariance matrix elements for $FSAr_n^+$ than for $AnAr_n^+$.

The final result to be fit by this simulation and modeling algorithm is the pattern in the mass distribution of $FSAr_n^+$ cluster ions which shows local cluster population maxima at $\sim n = 4, 8, 20$. This behavior is consistent with a decrease in the Ar attachment rate at cluster sizes $n = 4, 8, \text{ and } 19$. We model this decrease for small clusters ($n < 15$) in the following way: $K_n = K(n+1)^z$ for $n < 4$, $K_n = 0.81K(n+1)^z$ for $4 \leq n < 8$, and $K_n = 0.73K(n+1)^z$ for $8 \leq n$. Results of this augmented simulation are displayed in Fig. 15. The best fit to

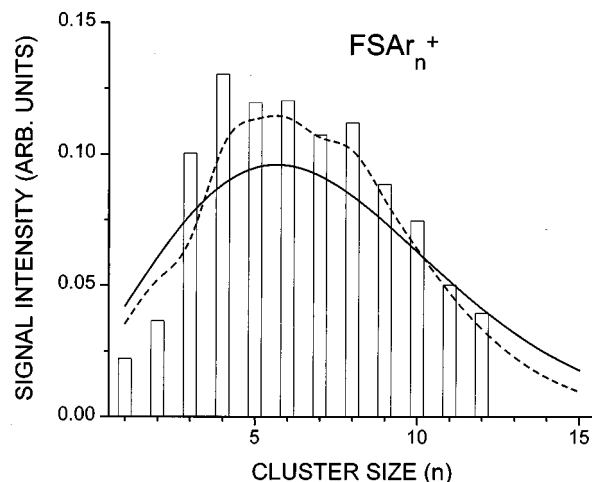


FIG. 15. The corrected measured (hollow bars) and simulated (solid and dashed lines) distributions of the FSAr_n^+ cluster ions produced at nozzle current lower than in Fig. 14 (but higher than in Fig. 13). The solid line shows the best fit without considering solvation shell or half-shell closing effects. The dashed line is obtained by simulating solvation shell or half-shell closing at cluster sizes 4 and 8 by lowering the cluster growth rates $K_{n \rightarrow n+1}$ by 19% for $n \geq 4$ and by additional 9% for $n \geq 8$.

the experimental data is obtained by varying parameters K/t_0 and $k_{0 \rightarrow 1}/k$ and by decreasing K_n at $n=4$ and 8 (dashed line, fitted parameters $K/t_0=4.1$, $k_{0 \rightarrow 1}/k=0.95$). This fit is compared in Fig. 15 with the best fit to the experimental data obtained without decreasing K_n (solid line, fitted parameters $K/t_0=3.9$, $k_{0 \rightarrow 1}/k=0.95$). Note that the value of K/t_0 for the distribution shown in Fig. 15 is lower than the K/t_0 fit to the cluster distribution shown in Fig. 14(c). This result is consistent with the lower valve current (pressure) for the data displayed in Fig. 15. With these rate decreases about the “magic” numbers, $n=4, 8$ the FSAr_n^+ cluster ion distribution is qualitatively fit. The drop in clustering rate at the “magic” cluster sizes would be consistent with the idea of solvent shell closing.

X. CONCLUSIONS

Covariance mapping of mass spectra is employed to study the dynamics of neutral cluster growth and ionic cluster fragmentation for the cluster systems T_mW_n , AnAr_n , and FSAr_n . Covariance mapping data provide central qualitative information about cluster growth and fragmentation. In order to achieve more quantitative understanding of the detailed cluster growth/fragmentation kinetics, modeling of covariance data and mass spectral intensities are quite useful.

The T_mW_n system is studied to test the covariance mapping technique for a system with weakly bound clusters and one in which neutral cluster growth, cluster ion fragmentation, and cluster ion chemistry occur simultaneously. Cluster fragmentation can be observed for this system if growth contributions to the correlation coefficients can be minimized. Nonetheless, the major contribution to the covariance comes from neutral cluster growth in this system as demonstrated by the correlation coefficient dependence on the ionization laser intensity I_L , or equivalently on the geometric mean of the signal intensities. In fact, modeling shows that fragmen-

tation makes a very small contribution to the covariance matrix elements, as is confirmed by the AnAr_n data for both one-color and two-color ionization, due to the low efficiency of the $I \leftarrow S_1$ ionization step. Thus the growth of neutral van der Waals clusters is the major contributing mechanism to the correlation coefficient and covariance matrix elements.

The reason the correlation coefficient is laser intensity dependent is that the variance matrix elements have different contributions than the covariance matrix elements: the variance is more dependent on Poisson fluctuations of total ion counts, which scale with I_L , than on the cluster growth contributions to total signal fluctuation behavior, which scale with I_L^2 .

These results compel us to define a normalized covariance that can eliminate the laser intensity or signal intensity product dependence of the usual covariance matrix elements: $\bar{C}([x^+],[y^+]) = C([x^+],[y^+])/[x^+][y^+]$. In this manner the normalized covariance that is growth dominated for these systems no longer depends on the signal intensities of the two ions correlated.

The AnAr_n^+ cluster ion distributions created by one-color and two-color ionization are very different due to the cluster ion fragmentation created by one-color ionization; nonetheless, their covariances are nearly identical because the dominant contribution to the covariance matrix elements comes from the growth process.

FSAr_n cluster ions are not fragmented by one-color ionization and their covariances are growth dominated. The mass spectral peak intensities have local maxima at $n \sim 4, 8$, and 20 for this system. The normalized covariance for FSAr_n shows that higher n maxima in the cluster ion distribution are generated from the lower n maxima by neutral cluster growth. The FSAr_n neutral cluster distribution appears to be a superposition of three broad, overlapping, log-normal-like distributions peaking around cluster sizes $n \sim 4, 8, 20$. Small random fluctuations of the parameters in the supersonic expansion shuffle intensity from one distribution node to another on a pulse-to-pulse basis. This is consistent with fast FSAr_n cluster growth kinetics. The maxima at $n \sim 4, 8$ and 20 could be due to solvation shell or half-shell closing.

For both AnAr_n and FSAr_n , kinetic modeling and computer simulations demonstrate that the dimer growth rates are an essential and controlling component of the growth process. The dimer growth rate appears to be larger for FSAr_n than for AnAr_n probably because FS has more low frequency vibrational modes that can couple to the van der Waals space and enhance the lifetimes of the dimer activated complex. The cluster formation rate constants for RAr_n , $n > 1$, clusters are also larger for FSAr_n than for AnAr_n .

The covariance mapping technique has proven extremely useful for the analysis of the underlying processes generating mass spectral data for van der Waals clusters: it has shown the importance of neutral cluster growth for the correlations between features in the cluster ion mass distribution. We are now applying this technique to the study of very different clusters (M_rO_s , Ag_rX_s systems) to determine the relative importance of cluster growth and fragmentation dynamics

for different systems and to explore the nature of the covariance matrix elements under very different limiting physical conditions.

ACKNOWLEDGMENTS

This work is supported in part by the USNSF and USARO. M. F. wishes to acknowledge Professor A. W. Castleman, Jr., for pointing out to him the early literature on covariance mapping.

- ¹(a) L. Q. Huang, R. J. Conzemius, G. A. Junk, and R. S. Houk, *Int. J. Mass Spectrom. Ion Processes* **90**, 85 (1989); (b) J. K. Schoer, R. S. Houk, R. J. Conzemius, and G. L. Schrader, *J. Am. Soc. Mass Spectrom.* **1**, 129 (1990).
- ²(a) L. J. Frasinski, K. Codling, and P. A. Hatherly, *Science* **246**, 1029 (1989); (b) *Phys. Lett. A* **142**, 499 (1989); (c) L. J. Frasinski, P. A. Hatherly, and K. Codling, *ibid.* **156**, 227 (1991); (d) L. J. Frasinski, M. Stankiewicz, P. A. Hatherly, G. M. Gross, K. Codling, A. J. Langley, and W. Shaikh, *Phys. Rev.* **46**, R6789 (1992).
- ³P. Jukes, A. Buxey, A. B. Jones, and A. J. Stace, *J. Chem. Phys.* **106**, 1367 (1997).
- ⁴D. A. Card, D. E. Folmer, S. Sato, S. A. Buzza, and A. W. Castleman, Jr., *J. Phys. Chem.* **101**, 3417 (1997).
- ⁵(a) M. R. Bruce, L. Mi, C. R. Sporleder, and R. A. Bonham, *J. Phys. B* **27**, 5773 (1994); (b) L. Mi, C. R. Sporleder, and R. A. Bonham, *Chem. Phys. Lett.* **251**, 252 (1996).
- ⁶(a) V. Berardi, S. Amoruso, N. Spinelli, M. Armenante, R. Velotta, F. Fuso, M. Allegrini, and E. Arimondo, *Int. J. Mass Spectrom. Ion Processes* **144**, 1 (1995); (b) V. Berardi, N. Spinelli, R. Velotta, M. Armenante, F. Fuso, M. Allegrini, and E. Arimondo, *Phys. Lett. A* **179**, 116 (1993); (c) S. Amoruso, V. Berardi, N. Spinelli, R. Velotta, M. Armenante, F. Fuso, M. Allegrini, and E. Arimondo, *Appl. Surf. Sci.* **86**, 35 (1995).
- ⁷S. Douin, J.-H. Fillion, M. Bonneau, P. Bréchnignac, D. Furio, D. Gauyacq, M. Horani, and N. Shafizadeh, *Chem. Phys. Lett.* **216**, 215 (1993).
- ⁸See, for example, B. R. Martin, *Statistics for Physicists* (Academic, New York 1971), Chap. 10.
- ⁹S. Li and E. R. Bernstein, *J. Chem. Phys.* **97**, 792 (1992).
- ¹⁰E. J. Bieske, A. S. Uichanco, M. W. Rainbird, and A. E. W. Knight, *J. Chem. Phys.* **94**, 7029 (1991).
- ¹¹(a) S. Douin, P. Parneix, F. G. Amar, and Ph. Bréchnignac, *J. Phys. Chem. A* **101**, 122 (1997); (b) P. Hermine, P. Parneix, B. Coutant, F. G. Amar, and Ph. Bréchnignac, *Z. Phys. D* **22**, 529 (1992).
- ¹²S. Piccirillo, D. Consalvo, M. Coreno, A. Giardini-Guidoni, S. Douin, P. Parneix, and Ph. Bréchnignac, *Chem. Phys.* **187**, 97 (1994).
- ¹³S. Douin, S. Piccirillo, and P. Bréchnignac, *Chem. Phys. Lett.* **273**, 389 (1997).
- ¹⁴See P. J. Robinson and K. A. Holbrook, *Unimolecular Reactions* (Wiley, New York, 1971).
- ¹⁵O. F. Hagen, *Surf. Sci.* **106**, 101 (1981), and references therein.